Chemotaxis as a navigation strategy to boost range expansion

https://doi.org/10.1038/s41586-019-1733-y

Received: 12 September 2018

Accepted: 3 October 2019

Published online: 6 November 2019

Jonas Cremer[1,2,5], Tomoya Honda[3,4,5], Ying Tang[1], Jerome Wong-Ng[1], Massimo Vergassola[1] & Terence Hwa[1,3]*

Bacterial chemotaxis, the directed movement of cells along gradients of chemoattractants, is among the best-characterized subjects in molecular biology[1–10], but much less is known about its physiological roles[11]. It is commonly seen as a starvation response when nutrients run out, or as an escape response from harmful situations[12–16]. Here we identify an alternative role of chemotaxis by systematically examining the spatiotemporal dynamics of *Escherichia coli* in soft agar[12,17,18]. Chemotaxis in nutrient-replete conditions promotes the expansion of bacterial populations into unoccupied territories well before nutrients run out in the current environment. Low levels of chemoattractants act as aroma-like cues in this process, establishing the direction and enhancing the speed of population movement along the self-generated attractant gradients. This process of navigated range expansion spreads faster and yields larger population gains than unguided expansion following the canonical Fisher–Kolmogorov dynamics[19,20] and is therefore a general strategy to promote population growth in spatially extended, nutrient-replete environments.

Decades of quantitative studies have elucidated how molecular signalling modulates the random run–tumble motion of individual bacterial cells and moves them up chemoattractant gradients[1–7]. By contrast, the physiological role of chemotaxis remains much less understood[11]. Notably, many of the chemicals sensed by bacteria are also consumed by them[17,21]. Hence, cells not only follow the chemoattractants set by their environment, but also shape the spatial profile of attractant abundance and adjust their movement accordingly. In particular, even a small group of cells can form strong attractant gradients that drive cell movement[9,10,22–24]. Here we perform a quantitative, physiological study of bacterial chemotaxis by taking into account not only chemotaxis itself, but also cell growth and metabolic reactions that lead to the self-generated attractant gradients. We use a motile strain of *E. coli* K-12 for which the growth physiology has been extensively characterized[25]. As with other motile *E. coli* strains, motility in this strain is enabled by an insertion element that activates the expression of the motility machinery (Supplementary Text 1.1). When inoculated at the centre of a soft-agar plate, these cells swim and readily expand outwards via chemotaxis; migrating cells form a visible ring that propagates with a well-defined speed (Fig. 1a, b), in line with classical observations[12,17].

Bacterial expansion dynamics

To characterize this expansion process quantitatively, we first investigated the dependence of expansion speed on the state of cell growth. We used medium containing saturating amounts of a primary carbon source supplemented by small amounts of aspartate or serine as the chemoattractant (see Supplementary Table 1 and Supplementary Text 1 for strains and growth conditions). Growth rate was determined largely by the primary carbon source, with little contribution from the aspartate and serine supplements (Supplementary Table 2). Expansion speed was clearly affected by the carbon sources used (Extended Data Fig. 1a, Supplementary Table 3). This was not due to the chemotactic effect of these carbon sources, as different expansion speeds were obtained for cells growing in the same medium (glycerol + aspartate, Extended Data Fig. 1b), with different steady-state growth rates attained by titrating the uptake of glycerol[26], which is not an attractant[21] (Supplementary Table 2). The measured expansion speeds follow a common increasing trend with the batch culture growth rate in the respective medium, with either aspartate or serine as the attractant (red and blue symbols, respectively; Fig. 1c). The same relation was also obtained for two other widely studied motile *E. coli* strains (Extended Data Fig. 1c), both of which harbour insertion elements that activate the expression of the motility machinery[27] (Supplementary Text 1.1). A more complex medium based on casamino acids that is commonly used in chemotaxis studies supports even faster growth and may be seen as an extension along the same general trend (orange symbols, Fig. 1c). By contrast, the expansion became much slower in the absence of a supplemented attractant, even if the primary carbon source was itself an attractant (for example, with glucose or aspartate only), and for a Δ*tar* mutant that cannot sense the attractant aspartate (Extended Data Fig. 1d).

The positive growth–expansion relation was unexpected in light of the widely held view—which is supported by gene expression data[14,25,28,29]—that bacterial chemotaxis is specifically triggered by nutrient shortage to find better environments[14,21,30]. To investigate the origin of this positive relation, we first characterized the swimming speeds of individual cells in different media by recording cell trajectories in well-mixed liquid culture devoid of chemotactic gradients

[1]Department of Physics, University of California at San Diego, La Jolla, CA, USA. [2]Department of Molecular Immunology and Microbiology, Groningen Biomolecular Sciences and Biotechnology Institute, University of Groningen, Groningen, The Netherlands. [3]Division of Biological Sciences, University of California at San Diego, La Jolla, CA, USA. [4]Present address: US Department of Energy, Joint Genome Institute, Berkeley, CA, USA. [5]These authors contributed equally: Jonas Cremer, Tomoya Honda. *e-mail: hwa@ucsd.edu

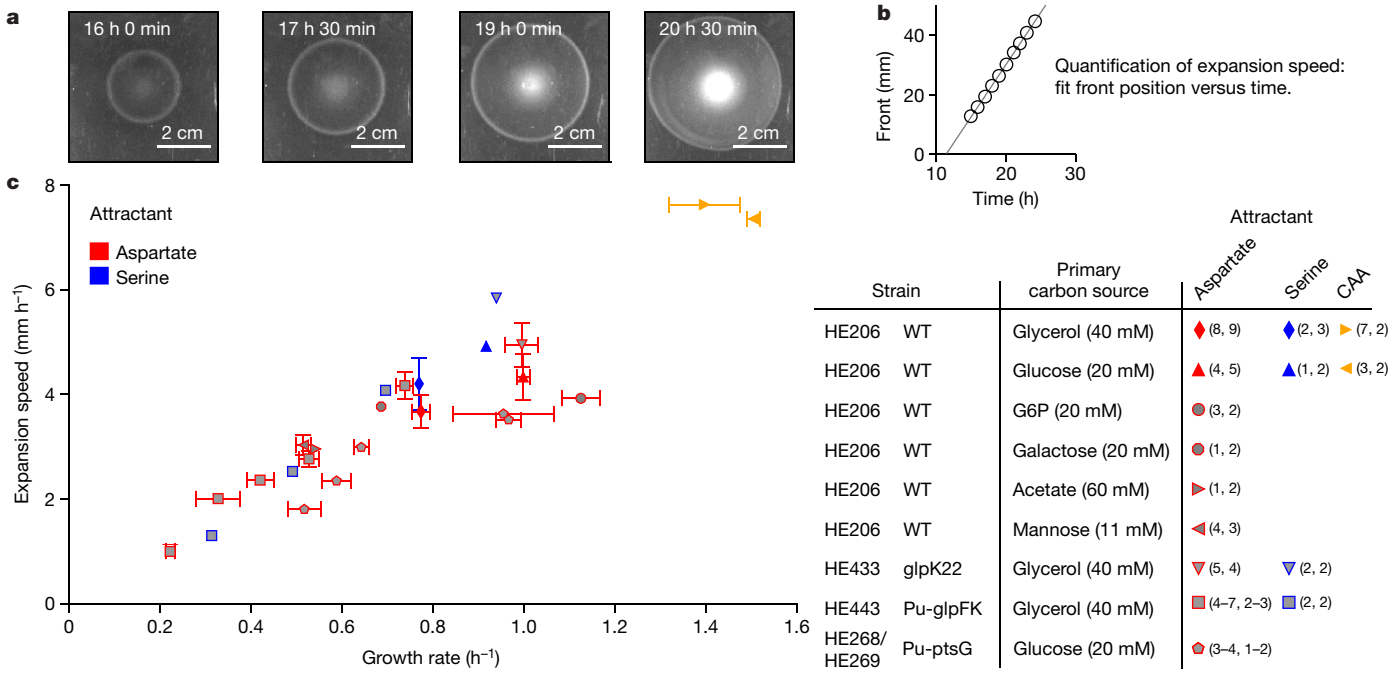

Fig. 1 | Growth dependence of expansion and swimming characteristics. **a**, Population of *E. coli* K-12 HE206 cells (wild-type (WT), see Supplementary Text 1.1) expanding in 0.25% soft agar with 40 mM glycerol and 100 μM aspartate. Photographs show population density at different times after inoculating exponentially growing cells at the centre of the agar plate. Rings indicate dense bacteria at the population front. Images are representative of experiments repeated independently three times. **b**, Tracking the ring position over time enables the precise quantification of expansion speed (slope). **c**, Expansion speed increases with growth rate. Expansion speeds are shown for HE206 cells (wild-type) in media with different primary carbon sources and for glycerol- and glucose-uptake mutants (HE433, HE443, HE268 and HE269) that grow at different rates on glycerol or glucose (as controlled by varying inducer levels; Supplementary Text 1.2), in combination with different attractants (100 μM aspartate, 100 μM serine or 0.05% casamino acids (CAA)), as indicated. CAA concentration was chosen to have the same aspartate and serine content as the medium with only aspartate or serine. Growth rates were measured in batch culture in the presence of attractant (Supplementary Text 1.4.2, Supplementary Table 2). Notably, these expansion speeds are much larger than those of the Fisher–Kolmogorov dynamics (no more than a few millimetres per hour; see below). Numbers in parentheses indicate number of biological replicates for growth and expansion speed measurements ($n_{\text{growth rate}}$, $n_{\text{expansion speed}}$). Mean ± s.d. (for $n \geq 3$) are shown.

(Supplementary Text 1.3). Consistent with previous reports[14,15], swimming speeds varied strongly in different growth phases (Extended Data Fig. 2a, b). However, such variations resulted from long adaptation periods during outgrowth from starvation, not from a transition out of exponential growth as commonly thought: for all of the *E. coli* strains that we tested, swimming speed remained high throughout steady exponential growth, but decreased rapidly upon entering starvation in both minimal and rich media (Extended Data Fig. 2c, d). Such behaviours, consistent with early findings[31], suggest that motility is instead favoured by *E. coli* during exponential growth. We next quantified swimming characteristics during exponential growth under different growth conditions, and found that neither swimming speed nor run duration showed substantial variation at different growth rates (Extended Data Fig. 2e, f). It follows that cellular 'diffusion' due to random movement resulting from run–tumble dynamics changed little over the broad range of growth rates examined (Extended Data Fig. 2g). Thus, the striking relation between expansion speed and growth rate in Fig. 1c is likely to be a property of the collective dynamics of the propagating population, rather than a direct consequence of single-cell characteristics.

To understand the collective expansion dynamics and its dependence on cell growth, we next observed the spatiotemporal dynamics of fluorescently labelled cells using confocal microscopy at both the population and single-cell levels (Fig. 2a). At the single-cell level, we characterized the random motion of cells in agar by tracking their trajectories over time (Extended Data Fig. 3a, b). The results, quantified by the effective cellular diffusion coefficients across different growth conditions examined, recapitulate the finding from liquid culture that the swimming characteristics are nearly independent of growth rate over the range examined (Extended Data Fig. 3c, orange symbols). At the population level, we quantified bacterial growth and density profiles over long distances across the entire agar plate. We first established that the growth of bacteria in agar is indistinguishable from that in batch culture (Extended Data Fig. 4a–c). Next, we analysed the time-lapsed radial density profiles of the expanding population in minimal medium, with glycerol as the primary carbon source and a low amount of aspartate as the attractant (Fig. 2b, Supplementary Video 1). The chemotactic ring was seen as a bulge in the density profile following the steep (exponential) increase at the front (Extended Data Fig. 4d). Notably, the advance of the front bulge (approximately 3.2 mm h^{-1}) was steadily followed by a trailing region with a broad, exponentially increasing density profile, suggesting that the outward migration of the ring was tightly coupled to the growth of bacteria behind the ring. This feature was also observed for a population in glycerol supplemented by serine or by aspartate and serine, and in complex medium (Fig. 2c, Extended Data Fig. 4e–h, Supplementary Videos 2–4), suggesting that the underlying dynamical phenomenon is independent of the nature of the attractant. By contrast, for wild-type cells grown in glycerol alone and for Δ*tar* cells grown in glycerol and aspartate, the much-reduced expansion speeds (Extended Data Fig. 1d) are accompanied by very different (flat) density profiles trailing the steep exponential rise, without recognizable density bulges (see top two panels of Fig. 2d, with full dynamics in Supplementary Video 1 (grey line)). As these populations do not chemotax, their expansion results from a combination of growth rate and random (diffusive) cell movement that can be modelled by the Fisher–Kolmogorov equation[32,33]. Detailed quantitative analysis established that the bacterial dynamics in these cases was described by the Fisher–Kolmogorov solution without adjustable parameters (Extended Data Fig. 5).

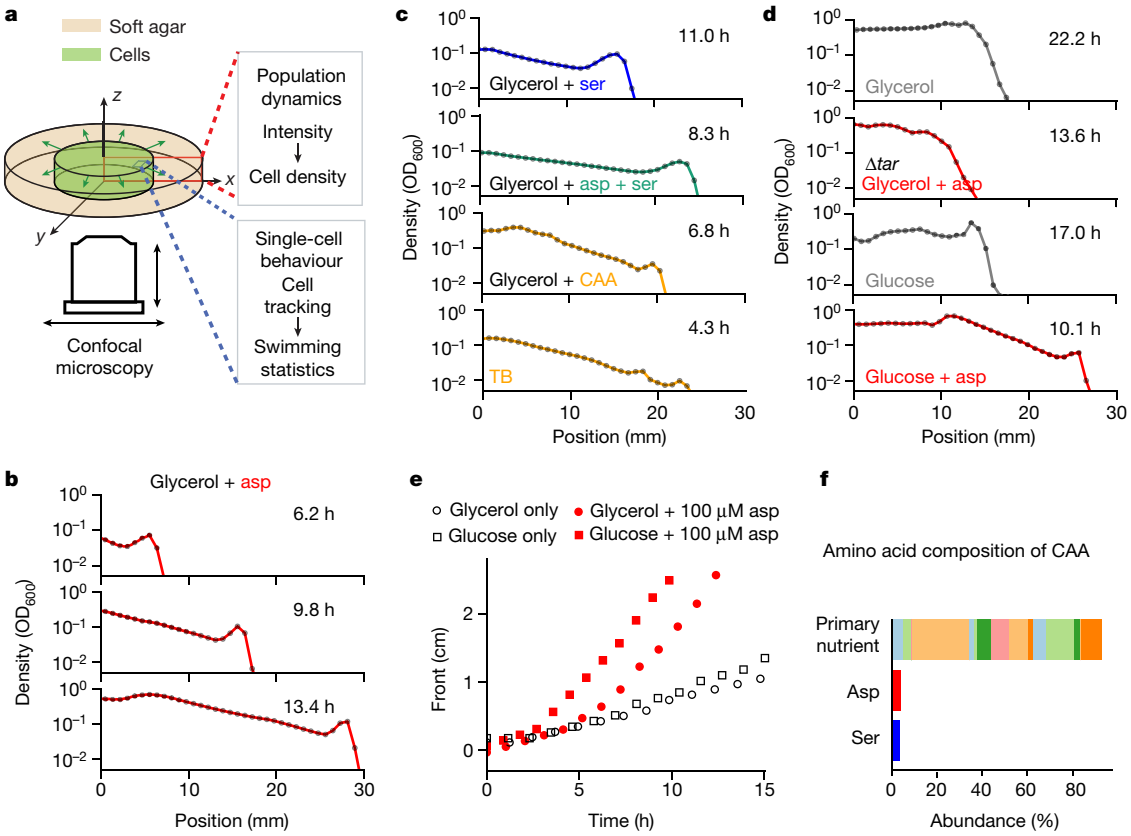

Fig. 2 | Density profiles of expanding bacterial population. a, Spatiotemporal evolution of the population in agar was obtained by quantifying the local fluorescence intensity of fluorescently labelled cells throughout the agar using confocal microscopy. Tracking of single cells enabled quantitative characterization of swimming behaviour at various positions and times in agar (Extended Data Fig. 3). **b**, Optical density profiles for fluorescent strain HE274 (wild-type) under reference conditions (40 mM glycerol + 100 μM aspartate (asp)) at different times, showing an advancing front marked by a density bulge and an exponential trailing region. See Extended Data Fig. 4d for the appearance of the same profiles on a linear density scale. **c**, Single-time density profiles for HE274 in other media with attractant(s), showing the same bulge(s) and trailing exponential region. Time-lapsed density profiles are shown in Extended Data Fig. 4e–h. **d**, No front bulge or trailing exponential region were seen for wild-type cells in 40 mM glycerol alone or for Δ*tar* cells (HE505) under reference conditions. A bulge without an exponential trailing region was seen for wild-type cells in 20 mM glucose alone, but a front bulge and a trailing exponential region appeared for wild-type cells in 20 mM glucose + 100 μM aspartate. **e**, Trajectory of front position against time for wild-type cells in 40 mM glycerol or 20 mM glucose, with or without 100 μM aspartate. Front positions are defined by thresholds in density (optical density at 600 nm (OD_{600}) > 0.002) from confocal scans. **f**, Illustration of our model of a complex medium: most nutrients are lumped together and treated as a 'primary nutrient' that fuels cell growth, with small amounts of major chemotactic components (here aspartate and serine). **b**–**e**, Experiments were conducted twice with similar observations for the reference condition (glycerol + aspartate) and once for other conditions.

Notably, even though glucose is an attractant[18,21], cells grown in a glucose plate exhibited a flat density profile following a bulge at the front (Fig. 2d (third panel), Supplementary Video 5), and the population expanded not much faster than in plates with glycerol alone (Fig. 2e, black symbols). Conversely, the combination of glucose and low amounts of aspartate again exhibited a distinct density profile with a broad exponential region trailing the front bulge (Fig. 2d (bottom panel), Extended Data Fig. 4i), along with much faster expansion dynamics (Fig. 2e, red squares). Thus, it appears that the combination of an abundant primary carbon source—regardless of whether it is itself an attractant—supplemented by low amounts of an attractant, is the minimal nutrient requirement to generate the type of behaviour that is generically encountered in rich media (Fig. 2f). Consequently, we adopted the simple medium used in Fig. 2b (glycerol + aspartate) as our model medium (reference condition) in our quantitative study.

The growth–expansion model

To describe the fast expansion dynamics in media with nutrient and attractant, we developed a mathematical model by extending the classical model of a propagating chemotactic ring by Keller and Segel[34,35]. The original Keller–Segel front was unstable given a realistic limit of chemotactic sensitivity[36]. Ingenious models proposed to remedy the problem[37–39] appear to be too restrictive to capture the simplicity and ubiquity of the observed ring propagation. We focus instead on the crucial role of bacterial growth in driving population expansion. Although the inclusion of growth in chemotactic models also dates back a long time[40,41], a satisfactory understanding under general conditions is still lacking[30,42] (Extended Data Fig. 6). Guided by our experiments, which established the distinct effects of a primary nutrient and a low amount of attractant on expansion (Figs. 1, 2), we explicitly modelled these two ingredients as separate dynamical variables driving bacterial growth and motility; see Fig. 3a for a summary of this growth–expansion (GE) model and Supplementary Text 2 for details.

To test the predictions of the GE model, we determined most model parameters directly by independent experiments in the reference condition, including growth rates in agar (Extended Data Fig. 4c), diffusion coefficients in agar (Extended Data Fig. 3c), and uptake rates of aspartate (Extended Data Fig. 7a–c); Supplementary Table 4 shows the full parameter list. With the molecular parameters available from the literature (Supplementary Text 2.4), only one parameter remained unknown: the chemotactic coefficient χ_0 (Fig. 3a). When we fixed this

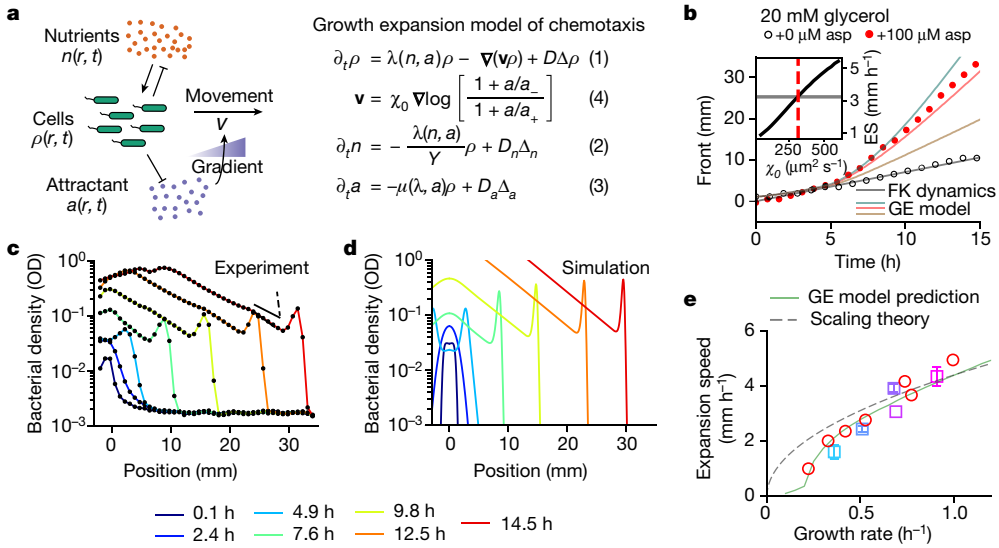

Fig. 3 | The growth–expansion model and its predictions. a, The coupled dynamics of growth and migration of the bacterial density, $\rho(r,t)$ is modelled by treating the concentrations of the major nutrient source and the attractant as two distinct variables, $n(r,t)$ and $a(r,t)$, with r being the radial distance from the centre. The dynamics of these variables are given by equations (1)–(3). The rate of cell growth $\lambda(n,a)$ and attractant uptake $\mu(\lambda,a)$ are fixed by our measurements (Supplementary Text 2.1). Nutrients and attractants diffuse with diffusion coefficients D_n and D_a, respectively. Y denotes the growth yield of the nutrient. Following the Keller–Segel model[34] and the coarse-grained description of chemotaxis[48], undirected swimming is described by a cell diffusion term, characterized by D. Directed movement is described by an advection term $\mathbf{v}$ that depends on local attractant gradients (equation (4)), with the chemotactic coefficient χ_0 as the proportionality factor. Other details of the model are described in Supplementary Text 2.1. **b**, The lone unknown parameter of the model χ_0 is fixed by adjusting the ratio χ_0/D such that the expansion speed of the model (black line, inset) matches the experimental observation (horizontal grey line, inset). The corresponding value of χ_0/D (red dashed line, inset) is used for other simulations. Solid red line shows the prediction of the GE model on front position at various times; it captures well the observed dynamics of front propagation of wild-type cells under reference conditions (red circles), including the crossover from Fisher–Kolmogorov dynamics (black circles and line, Extended Data Fig. 5). Solid green and brown lines show model predictions if χ_0/D was 30% larger or smaller, respectively. **c**, **d**, Observed (**c**) and simulated (**d**) density profiles at different times (coloured lines). The observed density bulges are less sharp than the simulated ones, owing in part to the limited spatial resolution of the data points (black dots). See Extended Data Fig. 3e for a finer view. Black solid line indicates the predicted slope of the trailing region (Extended Data Fig. 9a); dashed line shows the slope of Fisher–Kolmogorov dynamics for comparison (Extended Data Fig. 5). The fluorescent strain HE274 was used as the wild type in **b**, **c**; experiments were conducted twice with similar observations. **e**, Predicted and observed changes in expansion speeds when varying the growth rate with different glycerol uptake rate, using HE274, HE484 and HE486 (square symbols). For HE486, three different concentrations of the inducer 3-methylbenzyl alcohol (3MBA) were used. Data for HE274 ($n = 2$) represents a mean of two replicates; expansion speeds for HE484 and HE486 are shown as mean ± s.d. ($n = 3$ biological replicates) and growth rates from single experiments. Red circles, data from Fig. 1c (glycerol as carbon source). Dashed line, prediction by scaling theory (Extended Data Fig. 9) when changing only the growth rate. Solid green line, prediction of the full GE model, including the observed dependence of model parameters (for example, diffusion constant and uptake rate) on growth rate.

parameter by matching the asymptotic expansion speed of the model with the observed value under the reference condition (Fig. 3b, inset), the GE model quantitatively captured the main features of the population dynamics under the reference condition. The dynamics of the front position (Fig. 3b, red line) captures the data (red circles), including the overlap with Fisher–Kolmogorov dynamics (grey circles and line) at early times. The gross shape of the steady-state density profiles matches well with the experimental profile (Fig. 3c, d); in particular, the slope of the exponential trailing region (Fig. 3c, solid black line) is much flatter than predicted by Fisher–Kolmogorov dynamics (Fig. 3c, dashed black line). A zoomed-in analysis of the front region by using single-cell tracking allowed us to carry out additional comparisons regarding the details of the front region (Extended Data Fig. 3d–h). The model also adequately accounted for the dependence of the expansion speed on the attractant concentration, which has long been known to peak at a moderate level[43], for both glycerol and glucose as the primary carbon source (Extended Data Fig. 7d–f). Furthermore, the same model can quantitatively capture the slow expansion dynamics for the case in which the attractant is the sole nutrient (for example, glucose only; Extended Data Fig. 8).

We next applied the GE model to investigate the origin of the positive growth–expansion relation (Fig. 1c). Because the cell diffusion coefficient depends weakly on the growth rate (Extended Data Fig. 3c) whereas the attractant uptake rate yields a strong dependence (Extended Data Fig. 7c), the latter provides a possible rationalization of the positive growth–expansion relation. Indeed, faster depletion of attractant could naively be thought to allow the front to advance faster. However, this turns out not to be the case, as changing the uptake rate hardly affected the expansion dynamics, in agreement with model predictions (Extended Data Fig. 7g–i, Supplementary Text 2.2). The observed growth–expansion relation (Fig. 1c) can in fact be approximately accounted for within the GE model by just changing the growth rate while keeping all other parameters fixed (Fig. 3e, dashed grey line). Qualitatively, the faster expansion in richer medium results from higher cell density at the front bulge, which leads to faster depletion of the attractant (Extended Data Fig. 7j, k). More quantitatively, a simple scaling analysis captures the square-root form of the growth-rate dependence (Extended Data Fig. 9a–c), and a linear dependence on the chemotactic coefficient χ_0 (Extended Data Fig. 9d, which stands in contrast to the square-root dependence on χ_0 when the attractant is the sole nutrient; Extended Data Fig. 8k). The full model, including the observed growth-rate dependencies of the macroscopic parameters (Extended Data Figs. 3c, 7c) and assuming the independence of the molecular parameters (Supplementary Text 2.1.3), describes the observed data very well (Fig. 3e, green line), without any adjustable parameters. Less is known quantitatively about how serine alone or in combination with aspartate affects the chemotactic parameters. However, the existing data appear to be captured well by the square-root

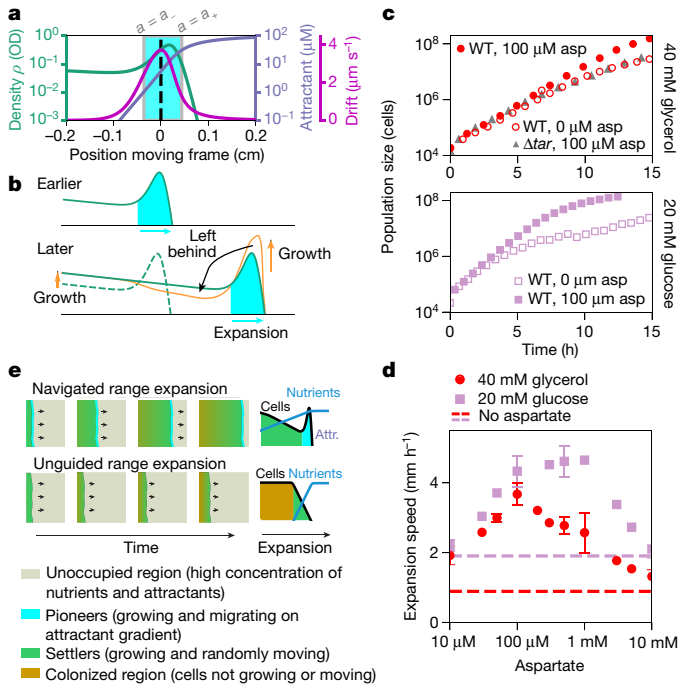

Fig. 4 | The expansion–colonization process. a, Spatial profiles of the density (ρ, green), attractant (a, mauve) and drift $|\mathbf{v}|$, purple) during steady migration in co-moving frame; dashed vertical line indicates the position of maximum drift. Highlighted area (cyan) indicates the region where the attractant concentration is in the range between a_- and a_+ (grey lines) in which the chemotactic response is maximal. Full spatiotemporal dynamics of the GE model is shown in Supplementary Video 6 for both the laboratory and co-moving frame. **b**, Illustration of the coupling between the front and trailing regions. Density profiles spaced by one doubling-time are shown. Orange line illustrates the density profile in a hypothetical case in which the effect of diffusion is turned off during this time. The difference (black arrow) represents the effect of cell transfers from the front to the gap right behind the front, which is mediated by diffusion. **c**, Size increase of populations expanding in glycerol or glucose quantified by confocal microscopy (Supplementary Text 1.4). Populations of wild-type cells (coloured symbols, strain HE274) increase faster with than without 100 μM aspartate as attractant. A slower increase is observed for a Δ*tar* mutant that cannot sense aspartate (grey triangles, strain HE505) even if aspartate was present. Differences between the size increases become noticeable after about 6 h, corresponding to the crossover from diffusive Fisher–Kolmogorov dynamics to navigated range expansion (Fig. 3b). Experiments for wild-type cells in glycerol + aspartate were conducted twice with similar results, others once; see also Supplementary Tables 2, 3. **d**, Expansion speed changing with attractant concentration. Wild-type cells (HE206) expanding in glycerol or glucose with varied aspartate concentration (Supplementary Table 9). Expansion speeds without additional attractant are shown as dashed lines. These results confirm previous observations[43] and can be quantitatively accounted for by the GE model (Extended Data Fig. 7e, f). Points represent means of $n \geq 2$ biological replicates, error bars (s.d.) shown when $n \geq 3$, see also Supplementary Tables 9, 10. **e**, Navigated mode of range expansion that involves chemotaxis (top) and unguided expansion (Fisher–Kolmogorov dynamics, bottom). Navigation along self-generated gradients of attractants (top) allows faster expansion. Remaining nutrients allow population growth behind the front. Right, corresponding density and nutrient or attractant profiles at the migrating front.

form when analysed separately for each attractant (Extended Data Fig. 1g), suggesting that different attractants and their combinations affect the magnitude but not the functional dependence of population expansion.

Further analysis of the GE model yields insights into how population growth and expansion are generated in a coordinated way. As indicated by the solution of the GE model (Fig. 4a) and confirmed by experimental observation (Extended Data Fig. 3g), cells in the front bulge region have positive drift velocities and move forward on average; they are the 'pioneers' of the population. Conversely, cells behind the bulge experience little chemotactic drift and can grow only locally; they are the 'settlers'. As the pioneers advance with the front and grow in number, some pioneers would remain behind owing to randomness in cellular motion (described by diffusion of cell density), effectively seeding the void region left behind by the propagating front (black arrow, Fig. 4b) for colonization in the future. This coupled expansion–colonization process is illustrated explicitly in Extended Data Fig. 9e using a discrete agent-based simulation that includes stochastic cell movement and division (see Supplementary Text 3). Cell-to-cell variations in swimming characteristics[5,24], which were not included in this calculation for simplicity, are expected to enhance further the transitions between the pioneers and the settlers.

Navigated range expansion

At the population level, the expansion–colonization process sustained by a primary nutrient source and low amounts of attractant provides an effective dispersal mechanism and a clear fitness advantage. This is illustrated by the observed gain in total population size on plates ('population fitness') during the expansion process (Fig. 4c). In glycerol medium supplemented with aspartate, the faster propagation of the population front (Extended Data Fig. 1e) accompanies the more rapid increase in total population size compared to a population seeded in the same medium without aspartate (filled and open red circles, respectively, Fig. 4c, top). This fitness advantage for the population is not due to the addition of aspartate as a nutrient supplement, because a Δ*tar* mutant that cannot respond to aspartate chemotactically (Fig. 2d) does not gain any fitness advantage from an aspartate supplement (grey triangles). Furthermore, the aspartate supplement substantially increases the population fitness even if the primary nutrient is itself an attractant such as glucose (purple squares, Fig. 4c, bottom). Thus, the fitness gain specifically requires an environment in which an attractant supplements an abundant primary nutrient source, regardless of whether the nutrient source is an attractant itself, reflecting the requirement for attaining a boost in expansion speed as established earlier (Extended Data Fig. 1e). This advantage of chemotaxis further relies on sufficiently low concentrations of the supplemented attractant (Fig. 4d). Notably, this requirement is at odds with the notion of cells seeking the attractant as a source of nutrients for growth and suggests instead that the supplemented attractant acts as a signalling cue to navigate and accelerate population expansion. Indeed, by separating the roles of nutrients and navigation cues, *E. coli* can use metabolites such as aspartate and serine that are rapidly taken up[44,45] as strong attractants without concerns for their poor ability to support growth (Supplementary Table 2), while maintaining fast growth on better nutrient sources such as glucose and glycerol.

In summary, chemotaxis along self-generated gradients of low-dose attractant supplements provides a local 'guide' for populations to expand rapidly into unoccupied territories, thereby giving them strong fitness advantages to grow in nutrient-replete environments. This navigated mode of range expansion (Fig. 4e, top) contrasts with the canonical, unguided mode of range expansion (Fisher–Kolmogorov dynamics[19,20,46], Extended Data Fig. 5) in which the population advances through the growth and random motion of cells at the front, leaving no nutrients behind the front (Fig. 4e, bottom). Notably, in navigated expansion, the guide is provided well before the population experiences any starvation. It thus manifests a built-in diversification strategy for a population with the 'foresight' to conquer new territories well before nutrients are depleted in the current environment. This foresight is important, because when starvation is experienced it is likely to be too late to turn on cell motility in order to facilitate effective population expansion (Extended Data Fig. 10).

The strategy of navigated range expansion in nutrient-replete conditions, analysed here for *E. coli* K-12 strains, is one of a number of ways in which chemotaxis can contribute to bacterial fitness. Under other conditions, chemotaxis can be used to respond to starvation or to escape from harsh environments such as non-optimal temperatures or pH ranges[14,15,21,30]. On the other hand, navigated range expansion, in which a diversified population of pioneers and settlers enables rapid occupation of open habitats for future colonization, might be used for range expansion by organisms other than bacteria. To efficiently guide the movement of the population along the desired direction for expansion, all that is needed is a component of the unoccupied environment that can be easily sensed and modified (for example, degraded but not consumed[47]); this is much easier for higher organisms to accomplish. Thus, navigated range expansion might also be used by higher organisms to rapidly colonize spatially extended habitats.

Online content

Any methods, additional references, Nature Research reporting summaries, source data, extended data, supplementary information, acknowledgements, peer review information; details of author contributions and competing interests; and statements of data and code availability are available at https://doi.org/10.1038/s41586-019-1733-y.

1. Berg, H. C. E. coli *in Motion* (Springer, 2004).
2. Alon, U., Surette, M. G., Barkai, N. & Leibler, S. Robustness in bacterial chemotaxis. *Nature* **397**, 168–171 (1999).
3. Sourjik, V. & Berg, H. C. Functional interactions between receptors in bacterial chemotaxis. *Nature* **428**, 437–441 (2004).
4. Bray, D. & Duke, T. Conformational spread: the propagation of allosteric states in large multiprotein complexes. *Annu. Rev. Biophys. Biomol. Struct.* **33**, 53–73 (2004).
5. Korobkova, E., Emonet, T., Vilar, J. M. G., Shimizu, T. S. & Cluzel, P. From molecular noise to behavioural variability in a single bacterium. *Nature* **428**, 574–578 (2004).
6. Tu, Y., Shimizu, T. S. & Berg, H. C. Modeling the chemotactic response of *Escherichia coli* to time-varying stimuli. *Proc. Natl Acad. Sci. USA* **105**, 14855–14860 (2008).
7. Sourjik, V. & Wingreen, N. S. Responding to chemical gradients: bacterial chemotaxis. *Curr. Opin. Cell Biol.* **24**, 262–268 (2012).
8. Tu, Y. Quantitative modeling of bacterial chemotaxis: signal amplification and accurate adaptation. *Annu. Rev. Biophys.* **42**, 337–359 (2013).
9. Waite, A. J. et al. Non-genetic diversity modulates population performance. *Mol. Syst. Biol.* **12**, 895 (2016).
10. Baym, M. et al. Spatiotemporal microbial evolution on antibiotic landscapes. *Science* **353**, 1147–1151 (2016).
11. Hein, A. M., Carrara, F., Brumley, D. R., Stocker, R. & Levin, S. A. Natural search algorithms as a bridge between organisms, evolution, and ecology. *Proc. Natl Acad. Sci. USA* **113**, 9413–9420 (2016).
12. Adler, J. Chemoreceptors in bacteria. *Science* **166**, 1588–1597 (1969).
13. Maeda, K., Imae, Y., Shioi, J. I. & Oosawa, F. Effect of temperature on motility and chemotaxis of *Escherichia coli*. *J. Bacteriol.* **127**, 1039–1046 (1976).
14. Amsler, C. D., Cho, M. & Matsumura, P. Multiple factors underlying the maximum motility of *Escherichia coli* as cultures enter post-exponential growth. *J. Bacteriol.* **175**, 6238–6244 (1993).
15. Staropoli, J. F. & Alon, U. Computerized analysis of chemotaxis at different stages of bacterial growth. *Biophys. J.* **78**, 513–519 (2000).
16. Paulick, A. et al. Mechanism of bidirectional thermotaxis in *Escherichia coli*. *eLife* **6**, e26607 (2017).
17. Adler, J. Chemotaxis in bacteria. *Science* **153**, 708–716 (1966).
18. Koster, D. A., Mayo, A., Bren, A. & Alon, U. Surface growth of a motile bacterial population resembles growth in a chemostat. *J. Mol. Biol.* **424**, 180–191 (2012).
19. Skellam, J. G. Random dispersal in theoretical populations. *Biometrika* **38**, 196–218 (1951).
20. Hastings, A. et al. The spatial spread of invasions: new developments in theory and evidence. *Ecol. Lett.* **8**, 91–101 (2005).
21. Adler, J., Hazelbauer, G. L. & Dahl, M. M. Chemotaxis toward sugars in *Escherichia coli*. *J. Bacteriol.* **115**, 824–847 (1973).
22. Saragosti, J. et al. Directional persistence of chemotactic bacteria in a traveling concentration wave. *Proc. Natl Acad. Sci. USA* **108**, 16235–16240 (2011).
23. Wong-Ng, J., Melbinger, A., Celani, A. & Vergassola, M. The role of adaptation in bacterial speed races. *PLOS Comput. Biol.* **12**, e1004974 (2016).
24. Fu, X. et al. Spatial self-organization resolves conflicts between individuality and collective migration. *Nat. Commun.* **9**, 2177 (2018).
25. Hui, S. et al. Quantitative proteomic analysis reveals a simple strategy of global resource allocation in bacteria. *Mol. Syst. Biol.* **11**, 784 (2015).
26. You, C. et al. Coordination of bacterial proteome with metabolism by cyclic AMP signalling. *Nature* **500**, 301–306 (2013).
27. Barker, C. S., Prüss, B. M. & Matsumura, P. Increased motility of *Escherichia coli* by insertion sequence element integration into the regulatory region of the flhD operon. *J. Bacteriol.* **186**, 7529–7537 (2004).
28. Liu, M. et al. Global transcriptional programs reveal a carbon source foraging strategy by *Escherichia coli*. *J. Biol. Chem.* **280**, 15921–15927 (2005).
29. Zhao, K., Liu, M. & Burgess, R. R. Adaptation in bacterial flagellar and motility systems: from regulon members to 'foraging'-like behavior in *E. coli*. *Nucleic Acids Res.* **35**, 4441–4452 (2007).
30. Lauffenburger, D., Kennedy, C. R. & Aris, R. Traveling bands of chemotactic bacteria in the context of population growth. *Bull. Math. Biol.* **46**, 19–40 (1984).
31. Adler, J. & Templeton, B. The effect of environmental conditions on the motility of *Escherichia coli*. *J. Gen. Microbiol.* **46**, 175–184 (1967).
32. Fisher, R. The wave of advance of advantageous genes. *Ann. Eugen.* **7**, 355–369 (1937).
33. Kolmogorov, A., Petrovsky, I. & Piscounov, N. Étude de l'équation de la diffusion avec croissance de la quantité de matière et son application à un problème biologique. *Mosk. Univ. Bull. Math.* **1**, 37 (1937).
34. Keller, E. F. & Segel, L. A. Model for chemotaxis. *J. Theor. Biol.* **30**, 225–234 (1971).
35. Keller, E. F. & Segel, L. A. Traveling bands of chemotactic bacteria: a theoretical analysis. *J. Theor. Biol.* **30**, 235–248 (1971).
36. Novick-Cohen, A. & Segel, L. A. A gradually slowing travelling band of chemotactic bacteria. *J. Math. Biol.* **19**, 125–132 (1984).
37. Budrene, E. O. & Berg, H. C. Dynamics of formation of symmetrical patterns by chemotactic bacteria. *Nature* **376**, 49–53 (1995).
38. Brenner, M. P., Levitov, L. S. & Budrene, E. O. Physical mechanisms for chemotactic pattern formation by bacteria. *Biophys. J.* **74**, 1677–1693 (1998).
39. Saragosti, J. et al. Mathematical description of bacterial traveling pulses. *PLOS Comput. Biol.* **6**, e1000890 (2010).
40. Nossal, R. Growth and movement of rings of chemotactic bacteria. *Exp. Cell Res.* **75**, 138–142 (1972).
41. Lapidus, I. R. & Schiller, R. A model for traveling bands of chemotactic bacteria. *Biophys. J.* **22**, 1–13 (1978).
42. Tindall, M. J., Maini, P. K., Porter, S. L. & Armitage, J. P. Overview of mathematical approaches used to model bacterial chemotaxis II: bacterial populations. *Bull. Math. Biol.* **70**, 1570–1607 (2008).
43. Wolfe, A. J. & Berg, H. C. Migration of bacteria in semisolid agar. *Proc. Natl Acad. Sci. USA* **86**, 6973–6977 (1989).
44. Prüss, B. M., Nelms, J. M., Park, C. & Wolfe, A. J. Mutations in NADH:ubiquinone oxidoreductase of *Escherichia coli* affect growth on mixed amino acids. *J. Bacteriol.* **176**, 2143–2150 (1994).
45. Yang, Y. et al. Relation between chemotaxis and consumption of amino acids in bacteria. *Mol. Microbiol.* **96**, 1272–1282 (2015).
46. Hallatschek, O., Hersen, P., Ramanathan, S. & Nelson, D. R. Genetic drift at expanding frontiers promotes gene segregation. *Proc. Natl Acad. Sci. USA* **104**, 19926–19930 (2007).
47. Seymour, J. R., Simó, R., Ahmed, T. & Stocker, R. Chemoattraction to dimethylsulfoniopropionate throughout the marine microbial food web. *Science* **329**, 342–345 (2010).
48. Celani, A. & Vergassola, M. Bacterial strategies for chemotaxis response. *Proc. Natl Acad. Sci. USA* **107**, 1391–1396 (2010).

Methods

No statistical methods were used to predetermine sample size. The experiments were not randomized and the investigators were not blinded to allocation during experiments and outcome assessment.

Strains used in this study

The reference strain for this study is HE206, a motile variant of an *E. coli* K-12 strain NCM3722 for which the physiology has been well characterized[25,26,49–52]. Similar to other motile *E. coli* strains that have previously been studied[27,53], the strain carries an insertion element upstream of the *flhDC* operon to enable motility. See Supplementary Text 1.1 for the strain context. Details on all used strains (deletion mutants, titratable carbon-uptake strains and fluorescently labelled strains) and their construction are provided. As indicated in the text, comparisons are made with MG1655 and RP437, other commonly used motile *E. coli* strains. All strains used in this study are listed in Supplementary Table 1.

Growth media

All growth media used in this study were based on a modified MOPS-buffered minimal medium[54]. Trace micronutrients were not added into the MOPS medium, as the metal components have been reported to inhibit motility of *E. coli*[31]. To change growth conditions, different carbon sources were supplemented in the medium. When indicated, CAA and tryptone broth (TB) were used. Minimal medium for the growth of RP437 involves four additional amino acids. For the strains with titratable carbon uptake (glycerol or glucose), 3-MBA was additionally provided as the inducer. Full details on medium composition and concentrations are provided in Supplementary Text 1.2.

Strain culturing and growth rate measurement

Growth measurements were performed in a 37 °C water bath shaker operating at 250 rpm. The culture volume was no more than 4.5 ml in 18 mm × 150 mm test tubes (Fisher Scientific) to limit the depth of the culture in the tube for aeration purposes. Each growth experiment was carried out in three steps: seed culture in LB broth, pre-culture, and experimental culture in identical minimal medium. For the seed culture, one colony from a fresh LB agar plate was inoculated into liquid LB broth and cultured at 37 °C with shaking. After 4–5 h, cells were centrifuged and washed once with the desired minimal medium. Cells were then diluted into the minimal medium and cultured in a 37 °C water bath shaker overnight (pre-culture). The starting OD_{600} in pre-culture was adjusted so that exponential cell growth was maintained overnight, preventing cells from reaching saturation. Cells from the overnight pre-culture were then diluted to OD_{600} = 0.005–0.02 in identical pre-warmed minimal medium, and cultured in a 37 °C water bath shaker (experimental culture). After cells had been grown at least for three generations, OD_{600} was measured around every half doubling of cell growth. At each time point, OD_{600} was measured by collecting 200 µl cell culture in a cuvette (Starna Cells) and using a spectrophotometer (Thermo Scientific). About 4–6 OD_{600} data points within the range 0.04 to 0.3 were used for calculating growth rate. All of the growth rates measured in this study are summarized in Supplementary Table 2.

Measurement of expansion speeds

Expansion speeds were measured using soft-agar plates containing 0.25% agar and growth media resembling the liquid culture conditions described above. Attractants were additionally provided and a detailed preparation protocol is provided in Supplementary Text 1.4. Expansion speeds were measured either by manual tracking of expanding ring positions over time (manual observation, ring position is clearly visible by eye) or by using confocal microscopy. For the manual observation, 15 ml of freshly prepared and still warm soft-agar medium was transferred into a Petri dish with a 10-cm diameter, resulting in a 2-mm-thick soft-agar layer. Agar was left to solidify for a minimum of 10 min at room temperature. For the confocal experiments, GFP-expressing plasmids were used as fluorescent markers, strains as indicated in the legends. Chloramphenicol (8 µg/ml) was additionally supplied into the soft-agar medium to maintain the plasmid. To prepare the soft-agar plates, 2.7 ml of the medium was transferred into a glass-bottom Petri dish (Ted Pella Inc.). The final thickness of the agar was approximately 1.2 mm. All plates were freshly prepared before the assay. To start the soft-agar assay (manual observation), 2 µl of cell culture from the (exponentially growing) experimental culture was transferred onto a pre-warmed soft-agar plate. The primary carbon source of the liquid culture was chosen such that it matched the growth conditions provided in the soft-agar plate. The plates were incubated at 37 °C. After the population covered a circular area of at least 2 cm in radius, the radius of the population (the front with chemotactic ring is clearly visible) was measured every 1–2 h for 4–6 time points. Expansion speeds were obtained as linear fits of the observed radii versus observation times (Fig. 1b). For convenience, the initial inoculation OD_{600} used for the manual assay was varied depending on culture conditions such that ring movements could be captured during the day. The expansion speeds examined in this study are listed in Supplementary Tables 3, 9, 10. For expansion observation and density scans using microscopy, cells were always inoculated at OD_{600} = 0.2 and observation was started immediately after the 2-µl cell culture was added to the agar. Expansion dynamics was analysed by looking at the emerging spatial intensity profiles. Details of confocal imaging, intensity analysis and calibration, and the determination of growth rates within soft-agar by confocal microscopy are provided in Supplementary Text 1.4.2–1.4.5. Custom-made code used is available via GitHub at https://github.com/jonascremer/chemotaxis_imageanalysisexpansiondynamics.

Measurements of swimming characteristics

To quantify the swimming behaviour of cells in liquid culture (no gradients), we grew cells as described above but with higher attractant concentrations to avoid the formation of temporal gradients (Supplementary Text 1.3.1). Polyvinylpyrrolidone was added to the medium to prevent cells from binding to surfaces and to protect flagella[55]. Sample volumes of about 200 µl were taken at different time points over the course of cell growth to quantify swimming behaviour (see Supplementary Text 1.3.1 for details on timing). Immediately after collection, samples were diluted to a lower OD_{600} of approximately 0.005 using filtered medium. The diluted sample was then used to load a rectangular capillary and cells within the capillary were observed by acquiring videos for 1 min, using a phase-contrast microscope. Using a custom-made Python script, cells were detected and cell trajectories were derived. Subsequently, cell trajectories were analysed to derive the swimming characteristics as previously reported[56]. Full details on data acquisition and analysis are provided in Supplementary Text 1.3. The code used is available via GitHub at https://github.com/jonascremer/swimming_analysis.

Cell trajectory analysis in soft agar

To quantify diffusion behaviour (undirected run and tumbling) and drift (directed run and tumbling) of swimming cells within the agar, we used time-lapse confocal microscopy to enable the detection and tracking of individual fluorescently labelled cells (Extended Data Fig. 3). The measurement enables the spatiotemporal resolution of swimming behaviour within an expanding population. To optimize the tracking of single cells, the number of fluorescent detectable cells was adjusted by mixing fluorescent cells with non-fluorescent cells (carrying a non-fluorescence protein[57] to minimize physiological differences between strains). Detailed methods on image acquisition, cell tracking and the statistical analysis to derive diffusion coefficients and drift are given in Supplementary Text 1.5.

Measurements of aspartate uptake

To quantify aspartate uptake, cells were grown in minimal medium supplemented with different carbon sources and 800 μM aspartate. Samples were collected at different optical densities during steady-state growth and the aspartate concentration was determined using a calorimetric aspartate kit (ab102512, Abcam). Additional details are provided in Supplementary Text 1.2.2. The aspartate consumption rates measured in this study are summarized in Supplementary Table 7. For each growth condition, measurements were repeated twice.

The growth–expansion model

Full details of the growth–expansion model introduced in Fig. 3 are provided in Supplementary Text 2. This includes the specific biological motivations for different terms used in the equations, including the terms that describe attractant consumption and the nutrient-dependent local growth rate (Monod type dependence[58–60]). The drift term that describes the directed movement along sensed gradients features Weber's law[7,61], and response rescaling[62–64] and parameters were taken from published receptor characterizations[21,23,65,66]. Reflecting boundary conditions and initial conditions matching the experimental conditions were used; see Supplementary Text 2 for details and equations. Numerical solution of the partial differential equations used an implicit scheme using Python and the module FiPy[67]. Integration over time was performed with time steps $dt = 0.25$ s, and a grid resolution with spacing $dx = 10$ μm. Simulations were performed using custom-made Python code, which is available via GitHub at https://github.com/jonascremer/chemotaxis_simulation. Parameters used are provided in Supplementary File simulationparameters.txt; see also Supplementary Text 2.5 for additional information.

Reporting summary

Further information on research design is available in the Nature Research Reporting Summary linked to this paper.

Data availability

Major experimental data that support this study are provided in this manuscript or available via figshare repositories: https://figshare.com/articles/Confocal_intensity_scans_expanding_bacteria/9639209 (confocal expansion data) and https://figshare.com/articles/Swimming_in_liquid_culture/9643001 (swimming observation data). Simulation data can be generated with the provided simulation code. Simulation parameters are provided in a separate file. The Supplementary Text provides additional details on strains, experimental methods and modelling.

Code availability

Custom-made code is available via GitHub for the analysis of swimming characteristics (https://github.com/jonascremer/swimming_analysis), the analysis of expanding populations using confocal microscopy (https://github.com/jonascremer/chemotaxis_imageanalysisexpansiondynamics), and the numerical simulations of the growth–expansion model (https://github.com/jonascremer/chemotaxis_simulation).

49. Lyons, E., Freeling, M., Kustu, S. & Inwood, W. Using genomic sequencing for classical genetics in *E. coli* K12. *PLoS ONE* **6**, e16717 (2011).
50. Soupene, E. et al. Physiological studies of *Escherichia coli* strain MG1655: growth defects and apparent cross-regulation of gene expression. *J. Bacteriol.* **185**, 5611–5626 (2003).
51. Brown, S. D. & Jun, S. Complete genome sequence of *Escherichia coli* NCM3722. *Genome Announc.* **3**, e008795 (2015).
52. Basan, M. et al. Overflow metabolism in *Escherichia coli* results from efficient proteome allocation. *Nature* **528**, 99–104 (2015).
53. Parkinson, J. S. Complementation analysis and deletion mapping of *Escherichia coli* mutants defective in chemotaxis. *J. Bacteriol.* **135**, 45–53 (1978).
54. Cayley, S., Record, M. T., Jr & Lewis, B. A. Accumulation of 3-(N-morpholino) propanesulfonate by osmotically stressed *Escherichia coli* K-12. *J. Bacteriol.* **171**, 3597–3602 (1989).
55. Berg, H. C. & Turner, L. Chemotaxis of bacteria in glass capillary arrays. *Escherichia coli*, motility, microchannel plate, and light scattering. *Biophys. J.* **58**, 919–930 (1990).
56. Masson, J.-B., Voisinne, G., Wong-Ng, J., Celani, A. & Vergassola, M. Noninvasive inference of the molecular chemotactic response using bacterial trajectories. *Proc. Natl Acad. Sci. USA* **109**, 1802–1807 (2012).
57. Liu, W., Cremer, J., Li, D., Hwa, T. & Liu, C. An evolutionarily stable strategy to colonize spatially extended habitats. *Nature* https://doi.org/10.1038/s41586-019-1734-x (2019).
58. Shehata, T. E. & Marr, A. G. Effect of nutrient concentration on the growth of *Escherichia coli*. *J. Bacteriol.* **107**, 210–216 (1971).
59. Schellenberg, G. D. & Furlong, C. E. Resolution of the multiplicity of the glutamate and aspartate transport systems of *Escherichia coli*. *J. Biol. Chem.* **252**, 9055–9064 (1977).
60. Cremer, J. et al. Effect of flow and peristaltic mixing on bacterial growth in a gut-like channel. *Proc. Natl Acad. Sci. USA* **113**, 11414–11419 (2016).
61. Shimizu, T. S., Tu, Y. & Berg, H. C. A modular gradient-sensing network for chemotaxis in *Escherichia coli* revealed by responses to time-varying stimuli. *Mol. Syst. Biol.* **6**, 382 (2010).
62. Shoval, O. et al. Fold-change detection and scalar symmetry of sensory input fields. *Proc. Natl Acad. Sci. USA* **107**, 15995–16000 (2010).
63. Lazova, M. D., Ahmed, T., Bellomo, D., Stocker, R. & Shimizu, T. S. Response rescaling in bacterial chemotaxis. *Proc. Natl Acad. Sci. USA* **108**, 13870–13875 (2011).
64. Celani, A., Shimizu, T. S. & Vergassola, M. Molecular and functional aspects of bacterial chemotaxis. *J. Stat. Phys.* **144**, 219–240 (2011).
65. Vaknin, A. & Berg, H. C. Physical responses of bacterial chemoreceptors. *J. Mol. Biol.* **366**, 1416–1423 (2007).
66. Neumann, S., Grosse, K. & Sourjik, V. Chemotactic signaling via carbohydrate phosphotransferase systems in *Escherichia coli*. *Proc. Natl Acad. Sci. USA* **109**, 12159–12164 (2012).
67. Guyer, J. E., Wheeler, D. & Warren, J. A. FiPy: partial differential equations with Python. *Comput. Sci. Eng.* **11**, 6–15 (2009).
68. Dufour, Y. S., Gillet, S., Frankel, N. W., Weibel, D. B. & Emonet, T. Direct correlation between motile behavior and protein abundance in single cells. *PLOS Comput. Biol.* **12**, e1005041 (2016).
69. Keegstra, J. M. et al. Phenotypic diversity and temporal variability in a bacterial signaling network revealed by single-cell FRET. *eLife* **6**, e27455 (2017).
70. Frankel, N. W. et al. Adaptability of non-genetic diversity in bacterial chemotaxis. *eLife* **3**, e03526 (2014).
71. Müller, M. J. I., Neugeboren, B. I., Nelson, D. R. & Murray, A. W. Genetic drift opposes mutualism during spatial population expansion. *Proc. Natl Acad. Sci. USA* **111**, 1037–1042 (2014).
72. Möbius, W., Murray, A. W. & Nelson, D. R. How obstacles perturb population fronts and alter their genetic structure. *PLOS Comput. Biol.* **11**, e1004615 (2015).
73. Fusco, D., Gralka, M., Kayser, J., Anderson, A. & Hallatschek, O. Excess of mutational jackpot events in expanding populations revealed by spatial Luria–Delbrück experiments. *Nat. Commun.* **7**, 12760 (2016).
74. Weinstein, B. T., Lavrentovich, M. O., Möbius, W., Murray, A. W. & Nelson, D. R. Genetic drift and selection in many-allele range expansions. *PLOS Comput. Biol.* **13**, e1005866 (2017).
75. Mesibov, R., Ordal, G. W. & Adler, J. The range of attractant concentrations for bacterial chemotaxis and the threshold and size of response over this range. Weber law and related phenomena. *J. Gen. Physiol.* **62**, 203–223 (1973).
76. Fraebel, D. T. et al. Environment determines evolutionary trajectory in a constrained phenotypic space. *eLife* **6**, e24669 (2017).
77. Blattner, F. R. et al. The complete genome sequence of *Escherichia coli* K-12. *Science* **277**, 1453–1462 (1997).

Acknowledgements We thank C. Liu and X. Fu for initiating this study, and H. Berg, P. Cluzel, K. Fahrner, J. S. Parkinson, T. Pilizota, T. Shimizu, V. Sourjik and Y. Tu for discussions. This work is supported by the NIH (R01GM95903) through T. Hwa and the NSF Program PoLS (grant 1411313) through M.V. T. Honda acknowledges a JASSO long-term graduate fellowship award.

Author contributions J.C., T. Honda, M.V. and T. Hwa designed this study. Experiments were performed by T. Honda and J.C., with contributions by J.W.-N. and Y.T. in characterizing swimming. J.C. and T. Hwa developed the model, and J.C. and Y.T. performed the numerical simulations. All authors contributed to the analysis of experimental and simulation data. J.C., T. Honda, Y.T., M.V. and T. Hwa participated in the writing of the paper and the Supplementary Information.

Competing interests The authors declare no competing interests.

Additional information

Supplementary information is available for this paper at https://doi.org/10.1038/s41586-019-1733-y.

Correspondence and requests for materials should be addressed to T.H.

Reprints and permissions information is available at http://www.nature.com/reprints.

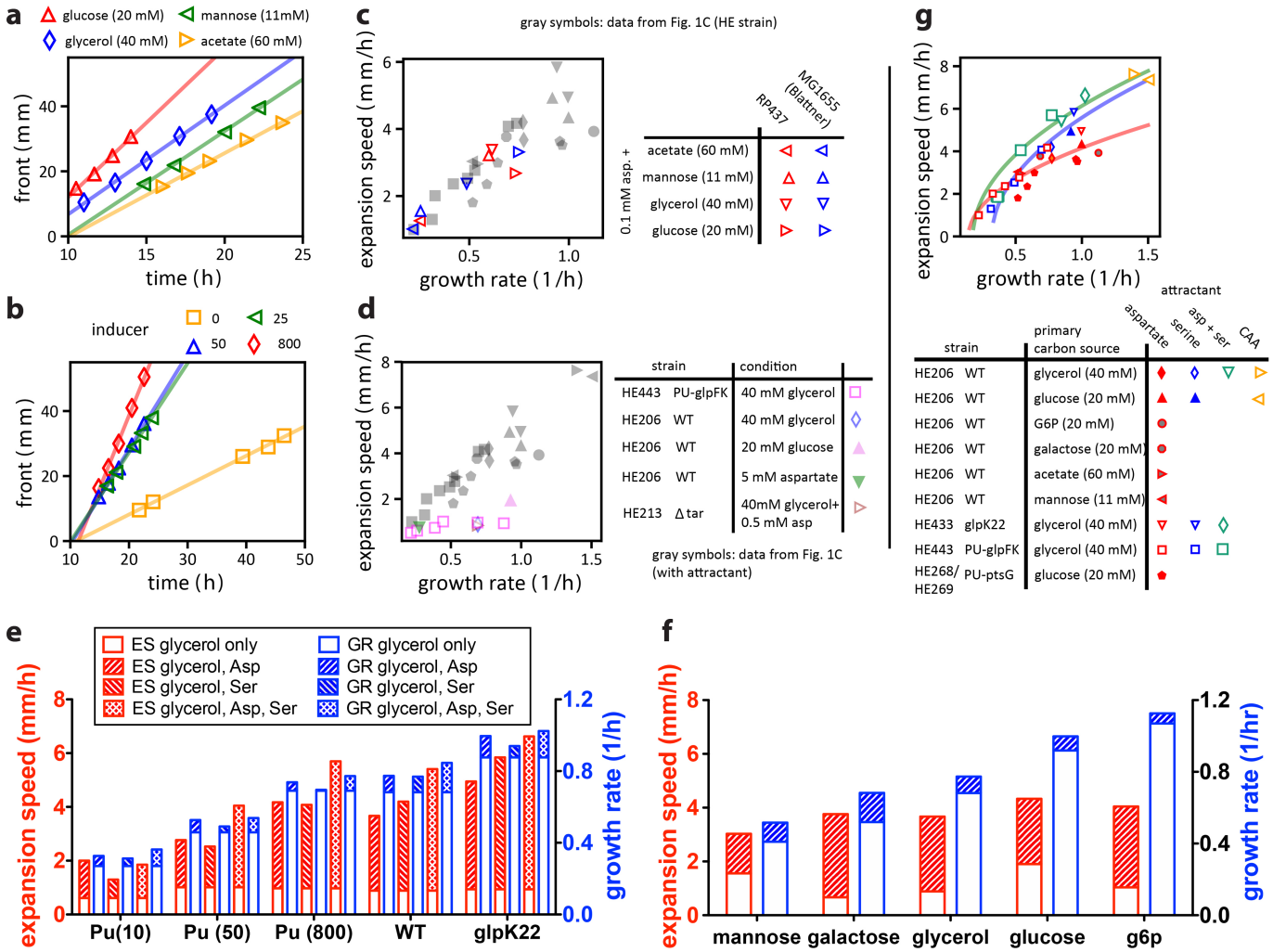

Extended Data Fig. 1 | Expansion speed measurements. a, Temporal evolution of front position for a population of *E. coli* HE206 cells (wild type) grown on a soft-agar plate with saturating amounts of different carbon sources (see legend) and 100 μM aspartate as attractant. Lines show linear fits. Experiments were repeated at least twice with similar results. **b**, Temporal evolution of front position for HE443 cells grown on 40 mM glycerol and 100 μM aspartate with different amounts of the inducer 3MBA (see legend) that titrate glycerol uptake[26], resulting in different growth rates (Supplementary Table 2). The experiments were repeated at least twice with similar results. **c**, Expansion speed and its dependence on growth rate for the commonly used *E. coli* K-12 strain MG1655B[77] (red symbols) and the K-12 variant RP437 (blue symbols) frequently used in motility studies (see Supplementary Text 1.1). Growth conditions were changed by varying the carbon source (from lower to higher growth rates: acetate, mannose, glycerol, glucose; see legend). Aspartate (100 μM) was added as the attractant. For the experiments with RP437, four amino acids (methionine, leucine, threonine, histidine) were provided at 1 mM each in the medium to sustain cell growth. Data from Fig. 1c are shown in grey for comparison. Data points represent the mean of two biological replicates, except for growth rates in acetate and mannose, which were from a single experiment. **d**, Expansion speeds plotted against the batch culture growth rate for populations grown in glycerol, glucose or aspartate as the only carbon source, without supplement of additional attractant (purple symbols). Growth on serine is very slow (<0.1 h^{-1}) and is not shown on the plot. Expansion speeds were much slower in these media without chemoattractant supplement, even though glucose and aspartate are both attractants themselves[21,45]. The same was observed for a Δ*tar* knockout strain when both glycerol and aspartate were present (open triangle). See Supplementary Tables 2, 3 for data values and sample sizes. Data from Fig. 1c are shown in grey for comparison. **e**, **f**, The difference between migration with and without additional attractant is further illustrated for growth on glycerol when growth rates are titrated (**e**), and for expansion when other carbon sources are provided (**f**). Hashed bars highlight additional increase in expansion speed (red) and growth rate (blue) when attractant is provided. In each case, supplementing low amounts of attractant(s) greatly increases expansion speed without affecting growth rate much. The graphs were created based on mean values listed in Supplementary Tables 2, 3. **g**, Expansion speed and its dependence on growth rate when two attractants are present (20 mM glycerol + 100 μM aspartate + 100 μM serine, green symbols) or for complex medium (CAA + carbon source, orange symbols). Data for single attractants (from Fig. 1c) are shown for comparison (20 mM glycerol + 100 μM aspartate, red; 20 mM glycerol + 100 μM serine, blue). Lines indicate fits to square-root dependencies as anticipated from a simple scaling analysis (Extended Data Fig. 9d). Data points in asp + ser (green points) represent means of two biological replicates ($n = 2$), except for growth rates of HE433 and HE443, which were from a single experiment ($n = 1$).

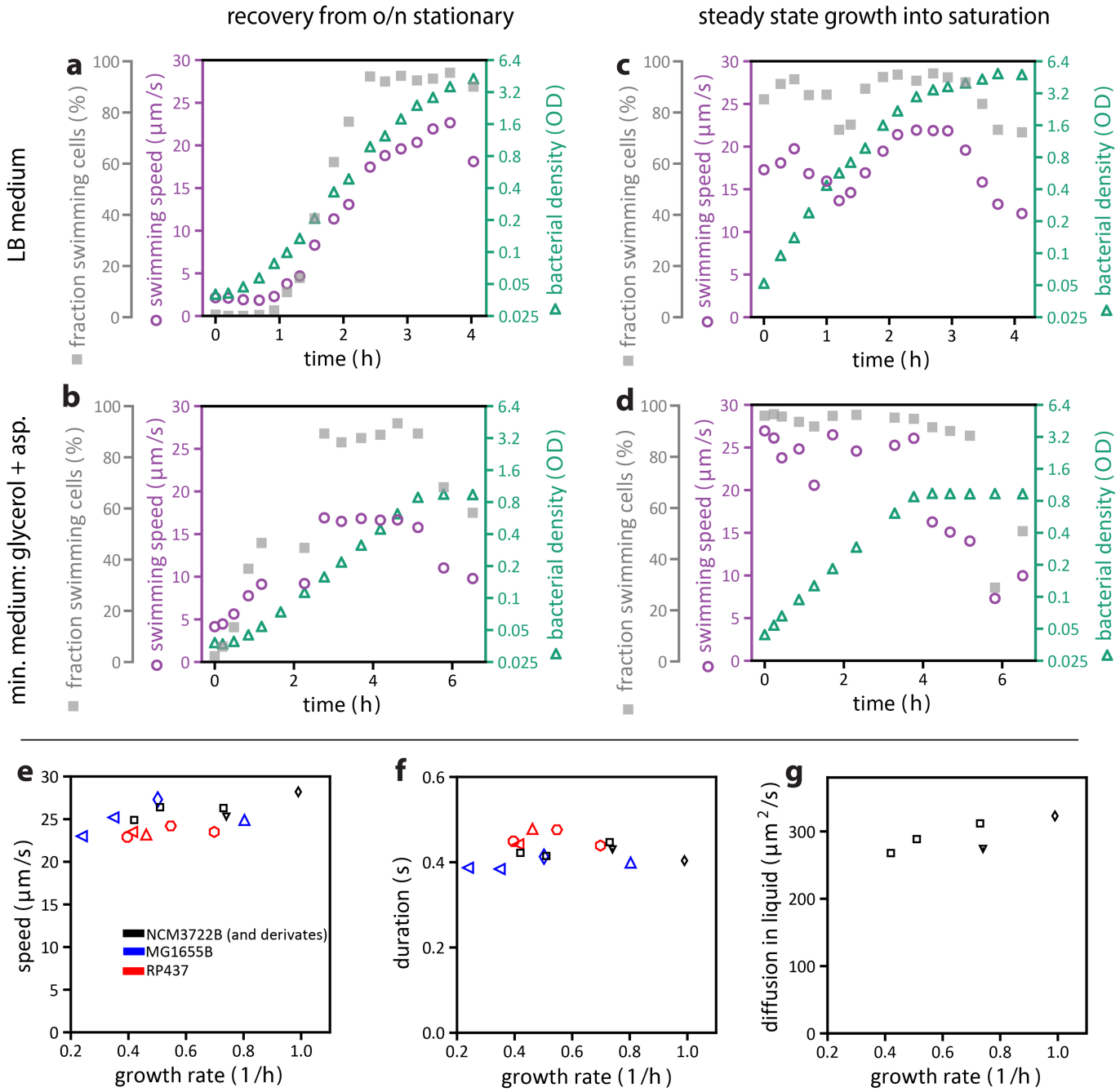

Extended Data Fig. 2 | See next page for caption.

Extended Data Fig. 2 | Swimming characteristics in liquid media (well-mixed conditions, no gradients). a–**d**, Average swimming speed (purple circles) and the fraction of motile cells (grey squares) were characterized for cells taken from batch cultures along a growth curve at different optical densities (OD_{600}; green triangles). For each condition, data points were collected from a single experiment. **a**, Culture was grown in LB medium, starting with an overnight LB culture that was sitting in saturation for 18 h before dilution into fresh LB medium at time zero. This experiment was essentially a repeat of previous work[14,15]; similar results were obtained, with motility increasing as growth progressed. Our data in the following panels suggest that most of the increase in swimming speed resulted from the increased fraction of motile cells in the first 2 h. **b**, Culture was grown in minimal medium with 10 mM glycerol and 1.7 mM aspartate, starting with an overnight pre-culture (same medium) that was in saturation for about 18 h before inoculation into fresh medium (time zero). As observed for LB (**a**), it took several hours for both the motile fraction and swimming speed to recover. **c**, Culture was grown in LB medium continuously for 10 generations, with bacterial density always kept below $OD_{600} = 0.5$ before dilution to fresh LB at time zero. Both the motile fraction and the swimming speeds are high in the exponential growth phase (0–2 h) except for a dip at an OD_{600} of approximately 0.5. Swimming speed and motile fraction decreased after the stationary phase was reached. **d**, Culture was grown in the same minimal medium (glycerol + aspartate) for about 20 generations, with bacterial density maintained below $OD_{600} = 0.6$ before measurement. As with LB (**c**), swimming speed and motile fraction remained high in the exponential growth phase (0–4 h) before sharply decreasing after entering the stationary phase. The strong variation of the fraction of motile cells observed here is in line with previous observations on cell-to-cell variation in swimming behaviour[68,69] and can strongly affect the dynamics of migrating populations[24,70]. **e**, **f**, Swimming behaviour observed in steady-state growth (as in **d** for the first ~3 h) for different (relatively fast) growth conditions and different *E. coli* strains (Supplementary Table 5). Swimming speeds (v) and durations between tumbling events (τ) obtained from trajectory analysis are shown in **e** and **f**, respectively. Black symbols show results for the NCM3722B-derived strains (HE206, HE433, HE443; growth at 37 °C) mainly used in this study. A similar weak dependence of quantities on growth was observed for MG1655B (red symbols, growth at 37 °C) and RP437 (blue symbols, growth at 30 °C). **g**, Estimated effective diffusion coefficient, $D = v^2\tau$, for the different growth conditions in NCM3722B-derived strains. **e**–**g**, Data points show the means of two biological replicates for HE433 and HE443 and the results of single experiments for HE206, MG1655B and RP437. See Supplementary Text 1.2, 1.3 for methods, Supplementary Table 5 for data values and conditions, and Supplementary Text 1.1 for strain details.

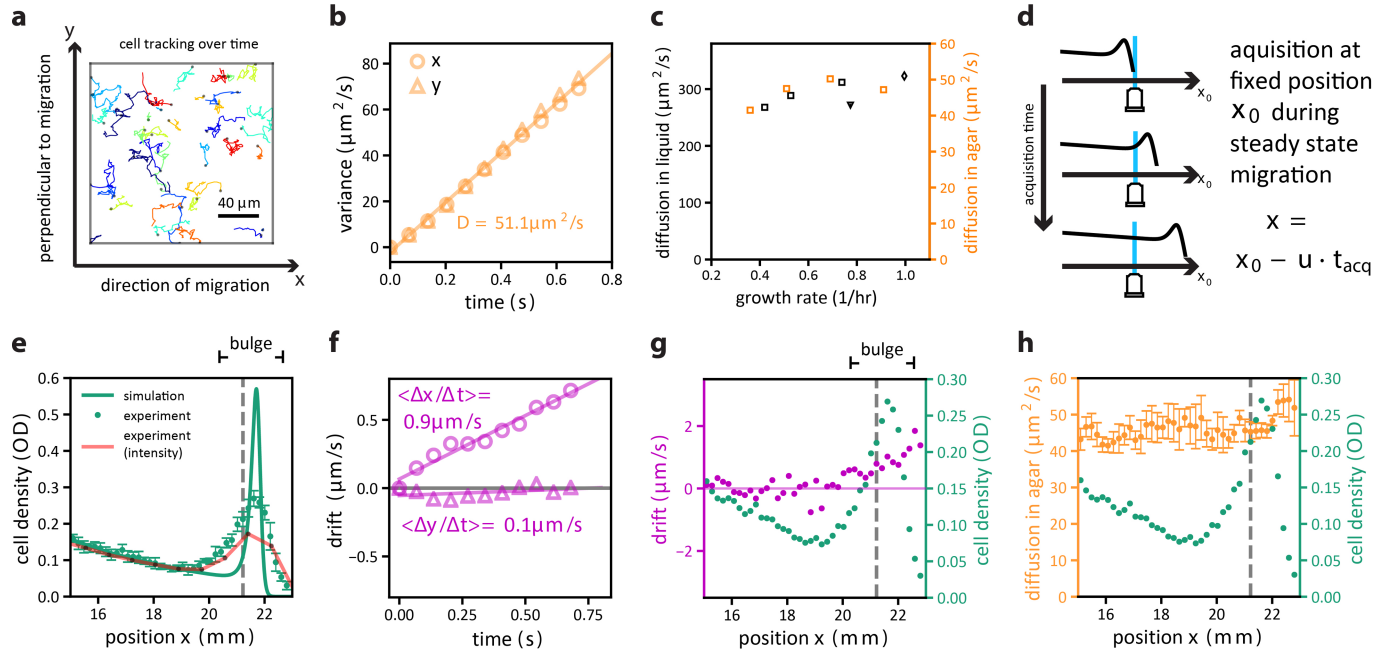

Extended Data Fig. 3 | Single-cell motility analysis in agar by confocal microscopy. Thirty-second videos allowing us to track the movement of single cells were acquired (see Supplementary Video 7 for an example). **a**, Example of trajectories derived from cell tracking analysis. Each colour indicates the trajectory of one cell over a span of on average 75 frames (5.1 s). **b**, Diffusive behaviour was obtained by a linear fit of displacement variance over time ($\mathrm{var}(\Delta x) = 2D\Delta t$). This analysis was performed for strain HE274 (wild type) growing in 40 mM glycerol and 100 µM aspartate (reference condition; Supplementary Text 1.5). Data shown here are for measurements in front of the expanding population (ahead of the density peak; however, the diffusion coefficient obtained at different locations does not exhibit much positional dependency, see below). Repeat of experiment showed similar results. **c**, Similar effective diffusion coefficients for swimming in soft-agar were obtained for other growth conditions (orange symbols; Supplementary Table 6) following the same trend as predicted from liquid culture measurements (black symbols, same as in Extended Data Fig. 2g). The diffusion measurements in soft agar were repeated twice with similar results. The data points represent means of two biological replicates. See Supplementary Table 6 for data values and conditions. **d**, To resolve cellular swimming behaviour of the expanding population at different spatial positions in the agar plate, videos allowing us to track single cells were acquired sequentially at a fixed position (of the agar plate) over time, for different acquisition times t_{acq} over which videos were taken (up to several hours for each position). Image direction x was aligned with direction of migration. In this setup, the migrating population (with speed u) passes the point of acquisition at a determined time, allowing us to determine the local drift speeds and diffusion coefficients relative to the front position: $x = x_0 - ut_{acq}$ (Supplementary Text 1.5). **e**, Density obtained by cell counting (green line) compared to population density obtained using the approach in Extended Data Fig. 4 (fluorescence scans, red line). The spatial resolution of the latter is much coarser, each measurement point being a black dot on the red line. For comparison, the simulation result (GM model, Fig. 3) is shown in green and moderately deviates from the measured profile. **f**, Analysis of average displacement along x (direction of migration) and y (direction perpendicular to migration) over time for an acquisition time t_{acq} corresponding to a position at the front bulge ($x = 21.3$ cm, indicated by the dashed lines in **e**, **g**, **h**). The average displacement (purple symbols) increased linearly in time along the direction of migration but was negligible perpendicular to the direction of migration (fitted purple lines show drift speed in each direction, $\langle \Delta x/\Delta t \rangle$ and $\langle \Delta y/\Delta t \rangle$). **g**, Position dependence of the drift (in the direction of expansion) was determined at different t_{acq}, corresponding to different positions of the expanding population. For ease of reference, cellular densities (**e**) are shown again as green symbols. Up to the resolution of the data, the drift velocity vanished to the left of the density trough ($x < 19$ mm). **h**, Position dependence of the diffusion coefficient. Using the approach from **b** to determine the diffusion coefficient at different t_{acq}, we obtained the results shown as orange symbols. A moderate (~20%) increase in D is observed at the very front of the population. This spatial dependence may be due to the accumulation of faster swimming cells at the front[9]. All data in **e**–**h** are from a single expansion experiment done under reference conditions (40 mM glycerol + 100 µM aspartate; 2:1 mixture of fluorescent variant HE274 and non-fluorescent variant HE339). Similar results were obtained for one biological replicate. Error bars in **e**, **h** denote s.d. and were calculated from repeated observations at three different times during the same expansion process.

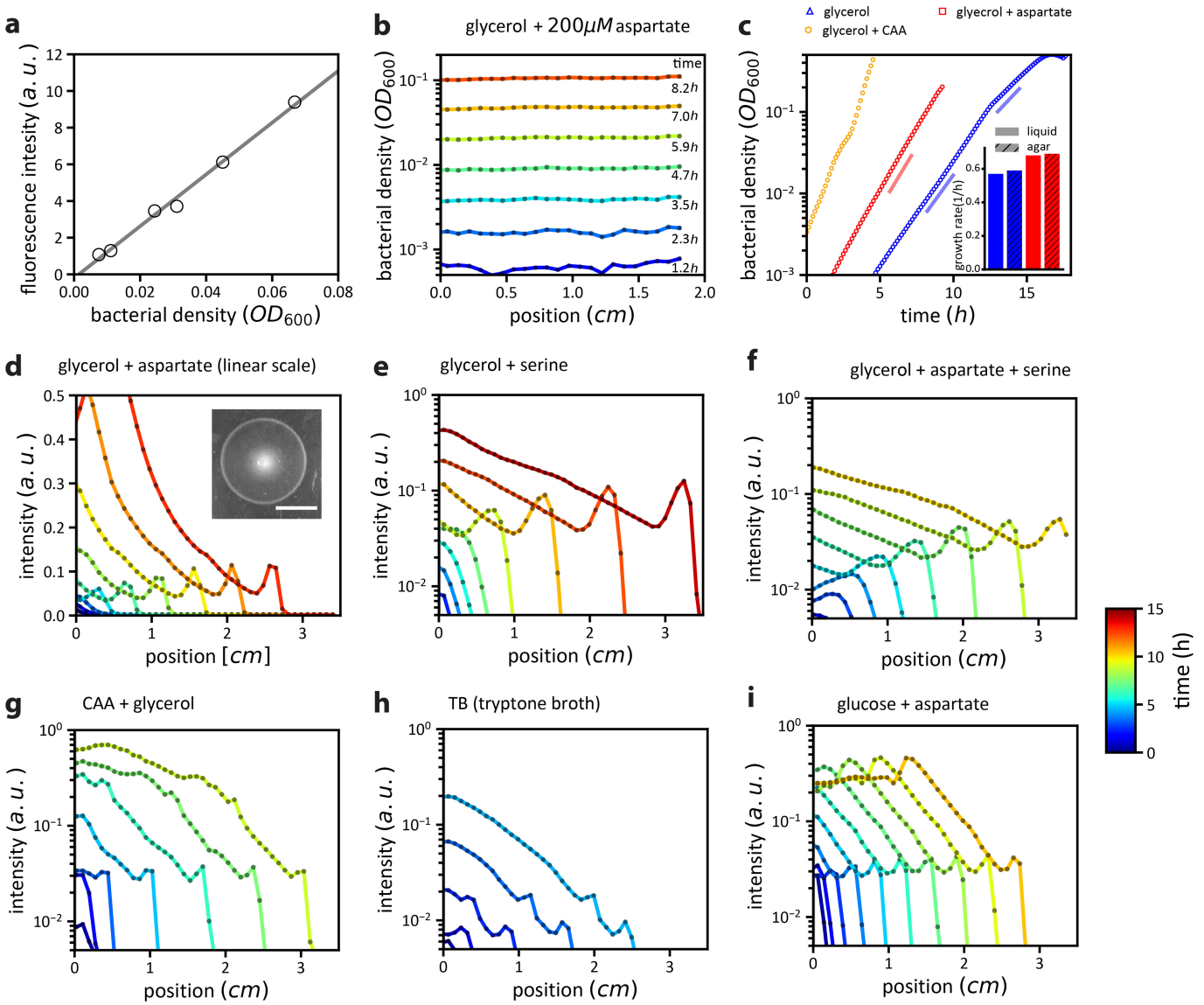

Extended Data Fig. 4 | Population-level observations of growth and expansion by confocal microscopy. Densities of bacteria growing in soft agar were determined at various times using confocal microscopy and fluorescently labelled cells; see Supplementary Text 1.4. **a**, Calibration of fluorescence intensity. Known numbers of cells were transferred from a batch culture to a fresh but cold soft-agar plate. After agar solidification (<10 min), intensity was measured. Fitted line gives relation between observed intensity (fluorescence integrated along the agar thickness) and cell density measured in batch culture (OD_{600}). **b**, Example of experiment to obtain growth rates in agar. Data are for strain HE274 (wild-type) grown in 40 mM glycerol and 200 µM aspartate. A small number of cells was mixed uniformly into fresh soft-agar plates. After agar solidification (<10 min), fluorescence intensity was observed over time. **c**, Derived growth curves in soft agar based on experiments as in **b**. Typically, there is a fast growth regime followed by a slower regime related to oxygen consumption and limitation for OD > 0.1: with oxygen running out, cells accumulate towards the agar surface and growth becomes slower. In this work, the population was always kept in the first aerobic regime. Growth rates in the first regime (coloured lines, Supplementary Table 2) were obtained by an exponential fit of the data and are comparable to those obtained in batch culture (inset). In **b**, **c** the experiment was conducted once. **d**, Photograph and spatiotemporal density profiles (linear intensity scale) for population expansion under reference conditions (glycerol + 100 µM aspartate; same data as in Figs. 1a, 2b). Scale bar, 2 cm. The confocal observations under reference conditions were repeated twice with similar results. **e**–**i**, Spatiotemporal density profiles (logarithmic density scale) for population expansion under different conditions, similar to those observed for the reference conditions (glycerol + 100 µM aspartate; **d**). Conditions are glycerol + 100 µM serine (**e**), glycerol + 100 µM aspartate + 100 µM serine (**f**), glycerol + 0.05% CAA (**g**), 1% tryptone broth (**h**), and glucose + 100 µM aspartate (**i**), all with strain HE274 (wild type). Colour scale bar applies to all panels. In **e**–**i**, the experiments were conducted once; expansion speeds were highly comparable to those measured manually.

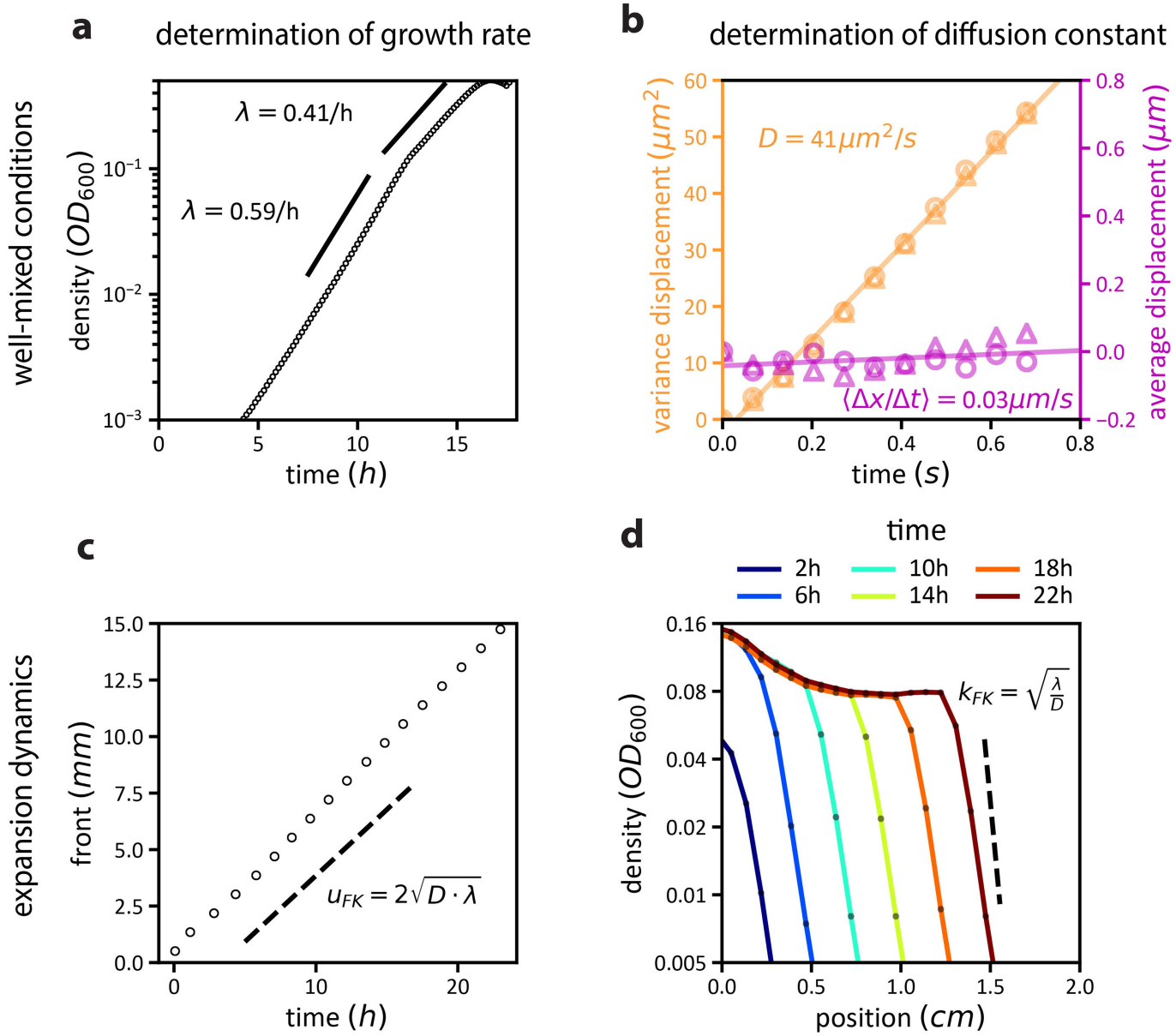

Extended Data Fig. 5 | Population expansion without attractant is quantitatively captured by Fisher–Kolmogorov dynamics. The Fisher–Kolmogorov dynamics is a canonical model to describe the dynamics of expanding populations[19,20]. It has been successfully used to investigate the expansion and evolution of non-moving bacteria at the front of dense bacterial colonies[46,71–74]. Here, we probe the Fisher–Kolmogorov dynamics and its validity to describe swimming bacteria. The Fisher–Kolmogorov dynamics is driven by population growth and undirected random motion (diffusion)[32,33]. To compare the predictions of Fisher–Kolmogorov dynamics to the expansion of a bacterial population in the absence of a chemoattractant, we thus independently quantified growth rates and cellular diffusion for cells homogeneously distributed in soft agar (**a**, **b**). We then compared the observed migration speed and the density profile of the migrating population (for growth on glycerol as the sole carbon source, as in Fig. 2d, top) with the Fisher–Kolmogorov predictions (**c**, **d**). **a**, Quantification of growth by measuring the temporal density increase of a homogeneously distributed population in agar (Extended Data Fig. 4a–c, Supplementary Text 1.4). Spatially averaged density increased exponentially with growth rate $\lambda = 0.59\ h^{-1}$ for densities <0.1 OD_{600}. For higher densities, the growth rate decreased but this regime is not important for the propagation of the front where density is low. **b**, Diffusion and drift of cells homogeneously distributed in soft agar. Analysis of recorded cell movement confirms the variance of position displacement to increase linearly in time (orange symbols) with diffusion constant $D = 41.5\ \mu m^2\ s^{-1}$ (linear fit of $\mathrm{var}(x) = 2D\Delta t$). In comparison, the average displacement of cells (purple symbols) and the calculated drift ($\langle \Delta x/\Delta t \rangle$, purple line) are small, indicating the absence of directed chemotactic movement. Data show average over three independent repeats (Extended Data Fig. 3, Supplementary Text 1.5). **c**, **d**, Front and spatiotemporal dynamics of an expanding population. **c**, Comparison of predicted expansion speed with the observed propagation of the population front. Position of the front $R(t)$ was determined from the observed cellular densities (threshold $OD_{600} < 0.005$); it increased linearly in time, that is, $R(t) = u_{obs}\,t$ with a speed $u_{obs} = 0.62\ mm\ h^{-1}$. Dashed line denotes predicted expansion speed calculated as $u_{FK} = 2\sqrt{\lambda \times D} = 0.59\ mm\ h^{-1}$. **d**, Density profile of the population front. Observed density profile can be fitted to an exponential dependence $\rho(r, t) \sim e^{-k_{obs}(r-R(t))}$ with $k_{obs} \approx 1.2\ mm^{-1}$. Dashed line indicates the slope of the exponential density profile predicted by the Fisher–Kolmogorov equation: $k_{FK} = \sqrt{\lambda/D} = 1.99\ mm^{-1}$. The discrepancy is likely to result from the low spatial resolution of the very sharp density drop; the exponential dependence of the experimental profile is defined by just three points. All experiments were conducted once with strain HE274 (wild type), using glycerol as the carbon source (no additional attractant, glycerol cannot be sensed). Growth and cell-tracking experiments were performed with uniform cell mixture in saturating glycerol conditions (40 mM). Expansion experiments were performed with 1 mM glycerol.

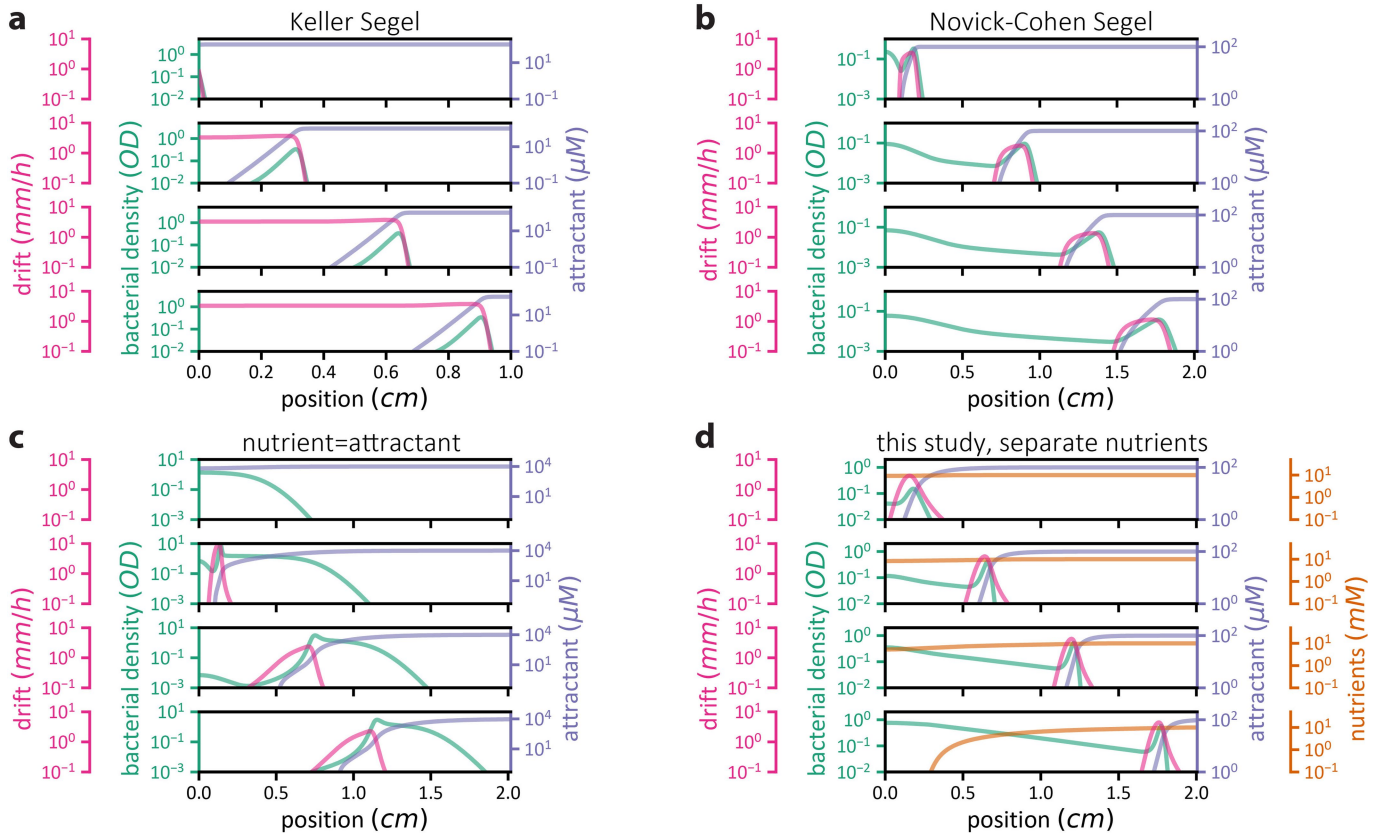

Extended Data Fig. 6 | Different models of chemotaxis-driven migration. To illustrate the difference among various models of chemotactic expansion, we show here simulation results of four different models. **a**, The classical model proposed by Keller and Segel[34] creates a self-generated attractant gradient owing to attractant consumption by the migrating population. It neglects cell growth (that is, $\lambda = 0$ in equation (3) in Fig. 3a), resulting in conservation of the total number of bacteria. It also assumes that the attractant gradient could be detected with infinite precision, such that log-sensing (Weber's law[75]) can be implemented by cells down to arbitrary low attractant concentrations, (that is, equation (4) with $a_- = 0$). The latter biologically unrealistic assumption introduces a singularity that pushes all bacteria forward at a steady migration speed, which is determined by the number of cells in the population, the conserved quantity. **b**, The model introduced by Novick-Cohen and Segel[36] fixed the singularity in the Keller–Segel model by imposing a minimal concentration for the sensing of attractant gradient (that is, equation (4) with $a_- > 0$). Owing to the lack of cell growth, the total number of bacteria is still conserved. In this model, the density of the front bulge decays over time because once bacteria diffuse out of the front, they lose the chemotactic gradient and cannot catch up with the front. The reduction in front density reduces the migration speed, which decays steadily towards zero. **c**, Model including cell growth that depends on attractant concentration (nutrient = attractant). Owing to growth, population size increases over time. However, as the attractant (nutrient) is mostly consumed at the front, there is not much growth behind the front and the trailing region behind the front is mostly flat. This scenario has been realized and analysed experimentally[18]; see Extended Data Fig. 8 for model details and discussion. **d**, The GE formulated in this study (Fig. 3a), including the chemotactic effect of an attractant, together with cell growth supplied by a major nutrient source. Front propagation of cells by chemotaxis is coupled to steady growth in the trailing region (see main text and Extended Data Fig. 9). Parameter values for all models are provided in Supplementary Table 8. For simplicity, simulations shown here were solved in one dimension (non-radial). Green lines denote bacteria density, blue lines denote attractant (or sole nutrient) concentration, brown lines denote concentration of nutrients (in addition to the attractant), purple lines show local drift (equation (4)).

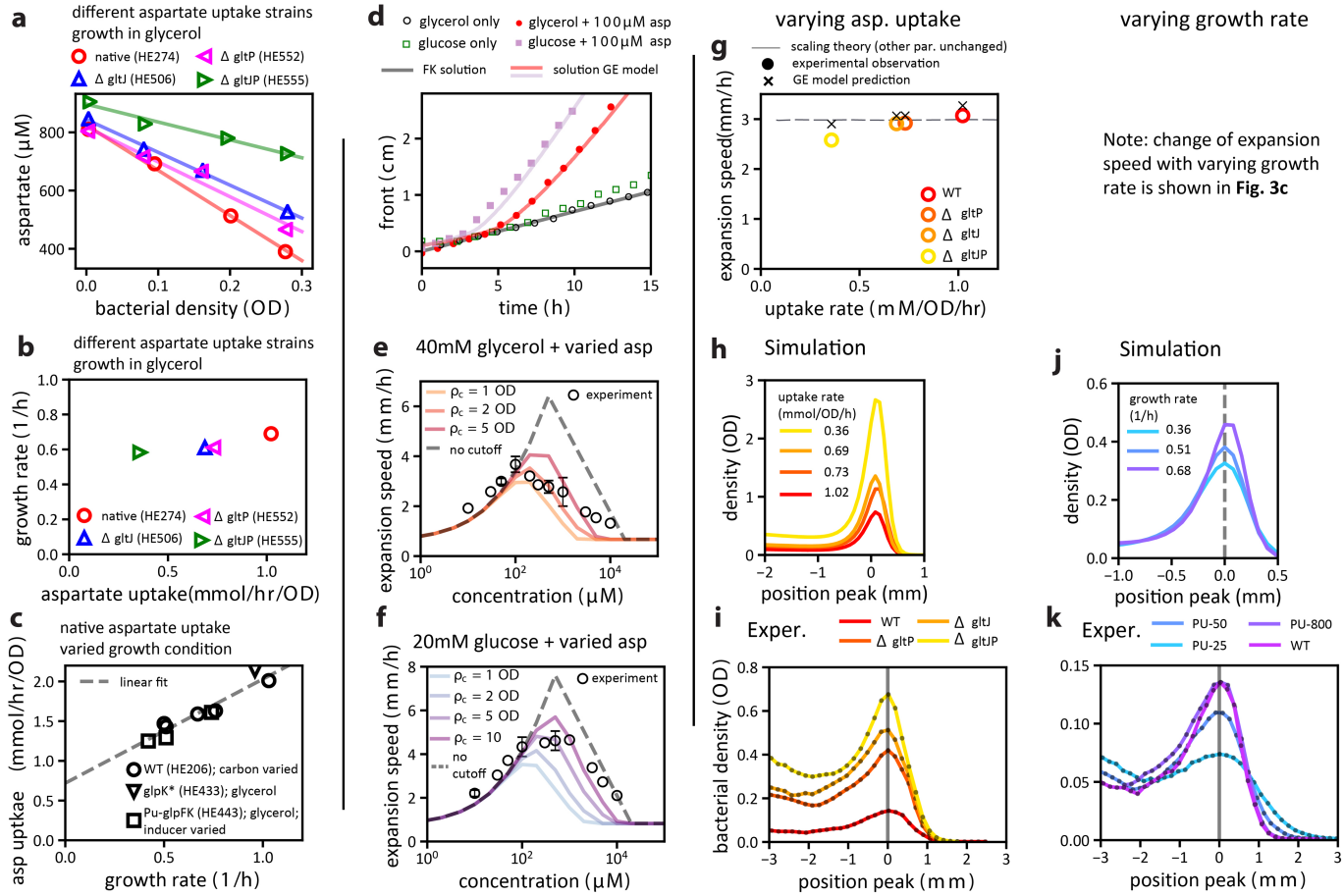

Extended Data Fig. 7 | Aspartate uptake and further analysis of expansion dynamics. a–**c**, Characterization of aspartate uptake for different growth conditions and strains. **a**, Aspartate uptake was determined using a colorimetric method to quantify remaining aspartate concentrations during growth (see Supplementary Text 1.2.3). In brief, change of aspartate concentration in the medium was measured during exponential growth at different cell densities (OD). Data are for growth with glycerol as the major carbon source (40 mM) and 0.8 mM initial aspartate concentration. Measurements for native aspartate uptake (wild type) and for different aspartate-uptake mutants (Δ*gltJ* and Δ*gltP* as well as the double mutant Δ*gltJP*). Lines show a linear fit. Uptake rate was determined by multiplying the obtained slope by the growth rate. **b**, The strains shown in **a** with different aspartate uptake rates exhibit similar growth rates. For each strain, the data points were collected from a single experiment. **c**, Dependence of aspartate uptake on growth rate for strains with native aspartate uptake. Growth is varied using wild-type cells (HE206, circles) grown on different sugar sources (acetate, mannose, glycerol or glucose), or by using the *glpK** mutant (HE433, triangle) or the glycerol titration mutant (HE443, squares), in glycerol with different levels of the inducer 3MBA (25, 50 or 800 μM). Aspartate (0.8 mM) was provided in each case for the measurement of aspartate uptake (see **a**). Line shows linear fit with parameters specified in Supplementary Text 1.2.3. **a**, **b**, Data obtained for strains carrying fluorescence plasmids. **c**, Data obtained for non-fluorescent strains (two biological replicates, means shown). Data, strain information and medium conditions including concentrations of carbon sources are provided in Supplementary Table 7. **d**, Expansion dynamics with glucose as the primary carbon source. The dynamics of the front, shown to be described well by the GE model in Fig. 3b in glycerol with aspartate, is examined with the primary carbon source being glucose (20 mM). In the presence of 100 μM aspartate, the observed front propagation dynamics (purple squares) is correctly captured by the GE model again (purple line), by merely replacing the growth rate by that in glucose ($\lambda = 1.0\ h^{-1}$) with no additional adjustment of the chemotactic coefficient χ_0. For reference, expansion is also shown for the condition in which no additional chemoattractant was provided (0 μM aspartate, open green squares), and the corresponding data for the condition in which glycerol was the primary carbon source (open black circles and corresponding lines from Fig. 3b). **e**, **f**, Dependence of expansion speed on attractant concentration with glycerol or glucose being the major nutrient. The increase in expansion speed at low attractant concentrations followed by decrease at higher concentrations, as previously observed[43], is qualitatively captured by the GE model (dashed grey lines) in both cases. A better quantitative agreement between model and data is obtained when the linear growth term in the GE model (equation (1) in Fig. 3a) is changed to the logistic form $\lambda\rho(1-\rho/\rho_c)$. Here ρ_c is the carrying capacity, introduced to capture saturation of cell density in the front bulge (Supplementary Text 2.3). Predictions by the model are shown for different carrying capacities as coloured lines. In line with the strict requirement for oxygen when growing on glycerol and the observation that cells at high density accumulate at the agar surface when expanding with glycerol as major nutrient source (data not shown), the carrying capacity needed to resemble the observations is much lower for glycerol (**e**) than for glucose (**f**). Data points represent means of biological replicates ($n = 2$ or more) with error bars (s.d.) shown for $n \geq 3$; see Supplementary Table 9 for data and sample sizes. **g**–**i**, Effect of varying aspartate uptake rate on expansion speed. The GE model predicts the expansion speed to be independent of the attractant uptake rate if all other parameters are kept fixed (**g**, dashed black line; Supplementary Text 2.2), with differences in attractant uptake compensated by changes in bacterial density at the front (**h**), such that the total rate of attractant depletion remains constant. This prediction was tested by characterizing the expansion dynamics of the aspartate-uptake mutants (strains HE506, HE552, HE555; Supplementary Text 1.1, Supplementary Tables 3, 7), which exhibited up to threefold difference in aspartate uptake (**a**), but only ~20% change in expansion speed (**g**). The small changes are readily accounted for by incorporating the small growth rate differences between these strains (**b**) into the GE model while keeping all other parameters fixed (**g**, green crosses). In addition, the aspartate-uptake mutants exhibited increasing peak densities at the front as predicted by compensation for reduced uptake (compare **i**, **h**). **j**–**k**, Predicted and observed changes in density profiles when varying the growth rate by titrating glycerol uptake in strain HE486 using 25 μM, 50 μM or 800 μM of the inducer 3MBA. For **g**, **i**, **k**, data were obtained from a single experiment for each strain and condition.

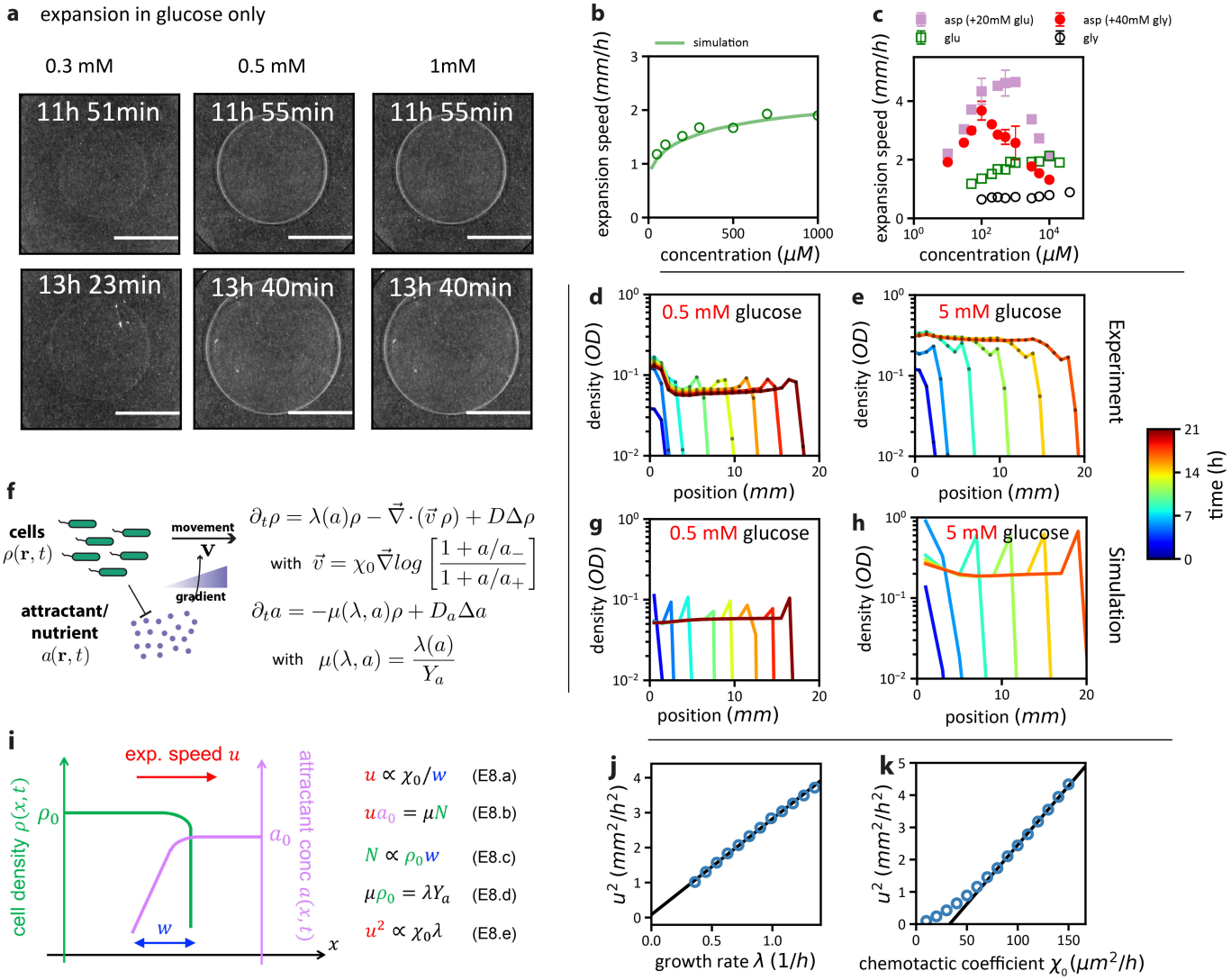

Extended Data Fig. 8 | See next page for caption.

Extended Data Fig. 8 | Expansion dynamics with the attractant being the sole nutrient source. This is one of the scenarios of chemotaxis investigated previously[18,76]. Here, for comparison with the dynamics presented in the main text, we show the expansion dynamics of populations grown with glucose (a chemoattractant[21]) as the sole carbon source. **a**, For wild-type cells (HE206) spotted on 0.25% agar plate with glucose as the sole carbon source, photographs show the existence of an outer ring at the front of the expanding population for a range of glucose concentrations. Scale bars, 2 cm. The experiments were repeated once with similar results. **b**, Dependence of expansion speed on glucose concentration. Intuitively, reducing the glucose concentration would be expected to increase the expansion speed, as it would take less time for the population to consume the attractant. However, the circles show that reducing the glucose concentration reduced population expansion speed. Data show means of two biological replicates. **c**, Direct comparison of concentration dependence of expansion speeds in glucose only (open green squares), glycerol only (open black circles), glycerol or glucose with aspartate (red circles, purple squares); data for latter same as shown in Fig. 4d and Extended Data Fig. 7e, f. Expansion speed in glucose (~1–2 mm h^{-1}) is faster than in glycerol (not an attractant) but well below the cases for which (low) amounts of attractants are supplemented. Shown data points represent means of biological replicates ($n = 2$ or larger), with error bars (s.d.) shown for $n \geq 3$; see Supplementary Tables 9, 10 for data and sample sizes. **d**, **e**, To understand the expansion behaviour, we used confocal scans to obtain the density profiles. The ring observed in the photograph is seen as a subtle density bulge at the front bounding a flat-density interior. Note the lack of an exponential trailing region, as observed when an attractant supplement is present (Fig. 2b, Extended Data Fig. 4i, photographs in Fig. 1a). The observed density profiles are comparable with those previously found with galactose as the attractant and the major nutrient source[18]. Experiments here were done with wild-type cells (HE206) (**a**–**c**) and fluorescence cells (HE274) (**d**, **e**). The confocal experiments were conducted once (expansion speeds are highly comparable to those measured manually). **f**, To capture the observed behaviours, we modified the GE model (Fig. 3a) using only one variable a to describe the attractant/nutrient. Consumption of the growth-enabling attractant is directly coupled to the increase in density via the yield Y. **g**, **h**, Fixing model parameters using available data for growth and chemotaxis on glucose (see Supplementary Text 2.4, 2.3 with parameters used listed in Supplementary Table 4), the model generated expansion speeds (green line in **b**) and density profiles that capture the experimental observations well; for comparison, a coarse-grained spatial resolution similar to the experiments was used to display the profiles obtained by the simulations. **i**, The model output can further be understood by a scaling analysis (Supplementary Text 2.6), resulting in the simple relation $u^2 \propto \chi_0 \lambda$ (equation (E8.e)). This relation is of the same form as the result of the Fisher–Kolmogorov dynamics, $u_{FK} = 2\sqrt{D\lambda}$ (see Extended Data Fig. 5), but with the chemotactic coefficient χ_0 replacing the diffusion coefficient D. **j**, **k**, The predicted dependence of u on λ and χ_0 (black lines) is validated by numerical simulations of the model (blue circles). The square-root dependence of the expansion speed on the chemotactic coefficient χ_0 stands in contrast to the linear dependence on χ_0 when an attractant supplement is provided (Extended Data Fig. 9d) and shows that the expansion dynamics with or without the attractant supplement are two distinct classes of mathematical problem. Note that the quantitative gain in expansion speed for the case with a supplemented attractant comes not only from the change in dependence on the chemotactic coefficient from $\sqrt{\chi_0}$ to χ_0, but also from the freedom to use attractants that have large χ_0 but small λ, which can be compensated by nutrients that give larger λ. Both aspartate and serine are strong attractants but poor nutrients, and are thus most potent when used in combination with a good nutrient source. Thus, separating the role of substances as nutrients and as cues not only relaxes the underlying mathematical constraint but also relaxes the biological constraint so that good attractants need not be good nutrients. These results provide an important support for the central thesis of this work, that chemotactic cells gain fitness by expanding in nutrient-replete conditions as a 'foresighted' navigation strategy (see main text).

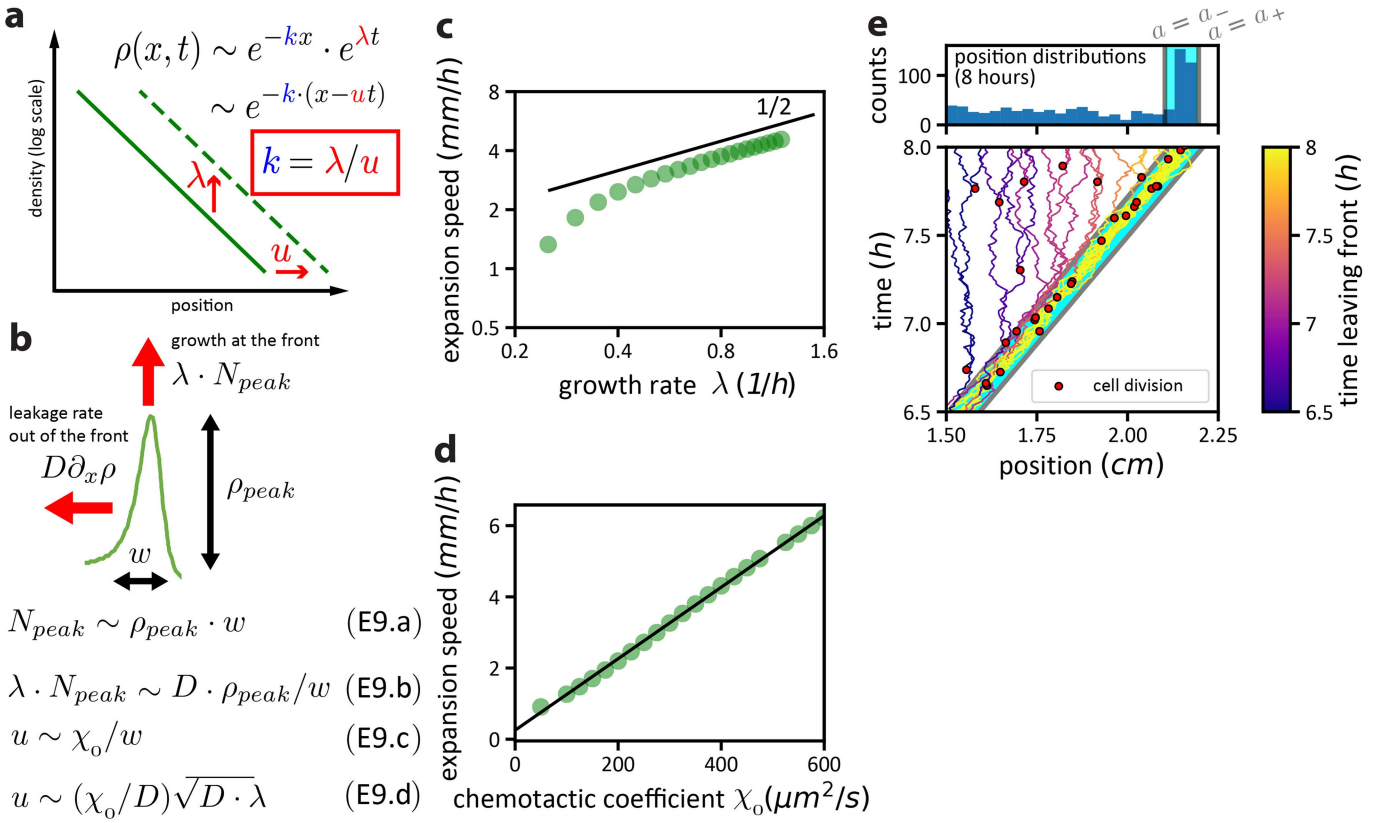

Extended Data Fig. 9 | Scaling analysis of expansion dynamics and illustration of the stochastic migration process. a, The exponential trailing region of the density profile is fixed by the cell growth rate λ and expansion speed u of the front. Because cells in the trailing region do not experience drift (Extended Data Fig. 3g), the apparent 'movement' of the trailing region at the same speed as the front bulge is possible only if it has an exponential profile, $\rho(r,t) \sim e^{k(r-ut)}$, with $k = \lambda/u$. **b**, Scaling of the expansion speed with model parameters. According to the GM model (Fig. 3a), the density peak at the propagating front is determined by a balance between cell growth and back diffusion (Fig. 4b). Using a crude scaling analysis to capture this balance, we can obtain (approximately) the quantitative determinants of the propagating speed. Consider a sharply peaked density bulge at the front, with peak density ρ_{peak} and width w. The number of cells contained in the peak region, N_{peak}, is given by the relation in equation (E9.a). Cell birth rate, λN_{peak}, is balanced by the back-diffusion flux, which is approximated as $D\rho_{peak}/w$, leading to the relation in equation (E9.b). To relate to the migration speed u, we note that around the density peak the drift speed v is nearly maximal (Fig. 4a), and equation (4) becomes $v_{max} \approx \chi_0 \frac{d}{dx}\ln(a)$. In the scaling approach, we take $u \sim v_{max}$ and the approximation $\frac{d}{dx}\ln(a) \sim 1/w$ leading to the relation in equation (E9.c). Combining equations (E9.a) and (E9.c), we obtain equation (E9.d) with the expansion speed increasing with the square-root of the growth rate λ. Note the χ_0/D factor appearing as a prefactor in the expression for u, which is responsible for the increase in the expansion speed in the presence of chemotaxis with respect to the Fisher–Kolmogorov dynamics (Extended Data Fig. 5) and for the dynamics with the attractant being the sole nutrient (Extended Data Fig. 8). **c**, **d**, Scaling results are confirmed by simulations of the GE model when varying growth rate λ (**c**) and chemotactic coefficient χ_0 (**d**). **e**, To further illustrate the intricate dynamics at the front of the expanding population, we performed stochastic agent-based simulations looking at the trajectories of single cells. Shown here are cell trajectories for a few selected cells located within the population front (pioneers) at time $t = 6.5$ h. Bottom, 38 trajectories with colour indicating the time the trajectory escaped from the front and cells switched from being pioneers to being settlers, which grow and colonize localities behind the front. Red circles indicate cell division events. Highlighted area (cyan) denotes front region with aspartate concentration in the range $a_- < a < a_+$. Top, position distribution of all simulated trajectories (1,000) at time $t = 8$ h. See Supplementary Text 3 for details.

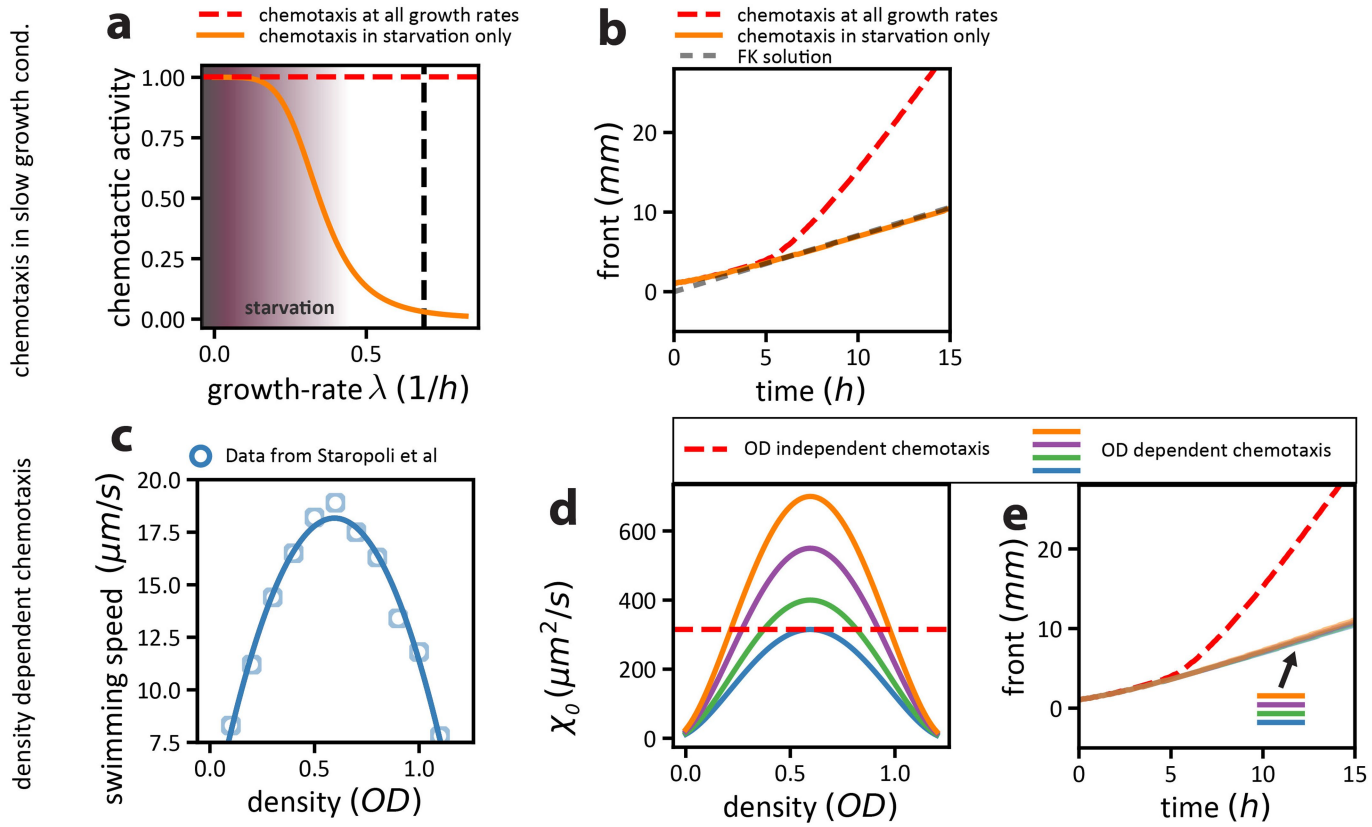

Extended Data Fig. 10 | Modelled scenario of chemotaxis as a strict starvation response. To examine the expansion characteristics of the population under the hypothetical scenario in which chemotaxis is a strict starvation response, we modified the GE model (Fig. 3a) to investigate the cases when chemotaxis is active either only in slow growth conditions (**a**, **b**) or within intermediate density ranges (**c**–**e**). **a**, To model chemotaxis being activated at slow growth, we introduced a strong dependence of chemotaxis on local growth rate (orange line). In contrast to the original GE model (dashed red line), we used a chemotactic coefficient that depends on growth conditions, $\chi_0 = \chi_0(\lambda(n))$ (orange line). Black dashed line shows growth rate in the presence of saturating glycerol. **b**, This dependence of chemotaxis on growth conditions leads to a marked decrease in the speed of expansion (compare orange and red dashed lines). The expansion dynamics of this model resembles the Fisher–Kolmogorov dynamics (grey dashed line), suggesting that chemotaxis does not boost population-level expansion when it is activated only under slow growth conditions. **c**–**e**, We further studied the case of swimming being a density-dependent response, active only at intermediate bacterial densities, as has been observed in batch culture measurements[15] (**c**). Taking such a dependence of the swimming speed (v) on the local cell density (ρ) and assuming $\chi_0 \sim v^2(\rho)$, we looked at the expansion dynamics for several maximum values of the chemotactic coefficient (**d**, **e**). For all of the forms of $\chi_0(\rho)$ shown in **d**, population expansion was slowed down substantially as compared to the reference case in which chemotaxis is also active at low densities (red dashed lines). The slow expansion dynamics is again similar to the Fisher–Kolmogorov dynamics, illustrating that the boost of expansion speed and population size by chemotaxis relies on chemotaxis being active at low densities. Note that in both cases analysed, we have not included the dependence of the diffusion constant on growth rate or local densities but assumed a constant value as in the original GE model. Introducing such dependences would further reduce the speed of expansion, below even that of Fisher–Kolmogorov dynamics. The origin of the slow expansion dynamics in these models is simple: a population cannot expand faster than its front, and the front is at low density and experiences the fastest growth rate.

nature research

Corresponding author(s): Terence Hwa

Last updated by author(s): Aug 22, 2019

Reporting Summary

Nature Research wishes to improve the reproducibility of the work that we publish. This form provides structure for consistency and transparency in reporting. For further information on Nature Research policies, see Authors & Referees and the Editorial Policy Checklist.

Statistics

For all statistical analyses, confirm that the following items are present in the figure legend, table legend, main text, or Methods section.

n/a	Confirmed	
☐	☒	The exact sample size (*n*) for each experimental group/condition, given as a discrete number and unit of measurement
☐	☒	A statement on whether measurements were taken from distinct samples or whether the same sample was measured repeatedly
☒	☐	The statistical test(s) used AND whether they are one- or two-sided *Only common tests should be described solely by name; describe more complex techniques in the Methods section.*
☒	☐	A description of all covariates tested
☒	☐	A description of any assumptions or corrections, such as tests of normality and adjustment for multiple comparisons
☐	☒	A full description of the statistical parameters including central tendency (e.g. means) or other basic estimates (e.g. regression coefficient) AND variation (e.g. standard deviation) or associated estimates of uncertainty (e.g. confidence intervals)
☒	☐	For null hypothesis testing, the test statistic (e.g. *F*, *t*, *r*) with confidence intervals, effect sizes, degrees of freedom and *P* value noted *Give P values as exact values whenever suitable.*
☒	☐	For Bayesian analysis, information on the choice of priors and Markov chain Monte Carlo settings
☒	☐	For hierarchical and complex designs, identification of the appropriate level for tests and full reporting of outcomes
☒	☐	Estimates of effect sizes (e.g. Cohen's *d*, Pearson's *r*), indicating how they were calculated

Our web collection on statistics for biologists contains articles on many of the points above.

Software and code

Policy information about availability of computer code

Data collection	Microscopic imaging data were collected and analyzed using the software LAS AF SP8 (Leica Microsystems) and a custom-made Python script (Python 2.7) available via GitHub (see code availability statement).
Data analysis	Custom made scripts were used to analyze experimental data and to perform simulations (full description in supplementary text). Scripts are available from the authors upon request.

For manuscripts utilizing custom algorithms or software that are central to the research but not yet described in published literature, software must be made available to editors/reviewers. We strongly encourage code deposition in a community repository (e.g. GitHub). See the Nature Research guidelines for submitting code & software for further information.

Data

Policy information about availability of data

All manuscripts must include a data availability statement. This statement should provide the following information, where applicable:

- Accession codes, unique identifiers, or web links for publicly available datasets
- A list of figures that have associated raw data
- A description of any restrictions on data availability

Major experimental data supporting this study are provided in this manuscript or available via figshare repositories: doi.org/10.6084/m9.figshare.9639209 (confocal expansion data) and doi.org/ 10.6084/m9.figshare.9643001 (data swimming observation). Simulation data can be generated with the provided simulation code and parameter sets.

Field-specific reporting

Please select the one below that is the best fit for your research. If you are not sure, read the appropriate sections before making your selection.

☒ Life sciences ☐ Behavioural & social sciences ☐ Ecological, evolutionary & environmental sciences

For a reference copy of the document with all sections, see nature.com/documents/nr-reporting-summary-flat.pdf

Life sciences study design

All studies must disclose on these points even when the disclosure is negative.

Sample size	Major quantities (growth-rate, expansion speed, swimming speed, and uptake-rates) in reference conditions confirmed small run to run variations (<10%, based on 3-9 biological replicates). Based on this finding we repeated most of the measurements shown in this study at least once (n=2 biological replicates). All repeats confirmed similar results. Confocal microscopy observations were conducted twice for the reference condition (glycerol+aspartate) showing again similar results. Microscopy observation were conducted once for other conditions.
Data exclusions	No data were excluded from the analysis.
Replication	All biological replicates showed comparable results.
Randomization	Not applicable.
Blinding	Data collection followed the same predetermined protocols throughout the whole study; the analysis of swimming behavior and imaging data is based on custom made codes without adjustable parameters. Blinding was therefore not used.

Reporting for specific materials, systems and methods

We require information from authors about some types of materials, experimental systems and methods used in many studies. Here, indicate whether each material, system or method listed is relevant to your study. If you are not sure if a list item applies to your research, read the appropriate section before selecting a response.

Materials & experimental systems

n/a	Involved in the study
☒	☐ Antibodies
☒	☐ Eukaryotic cell lines
☒	☐ Palaeontology
☒	☐ Animals and other organisms
☒	☐ Human research participants
☒	☐ Clinical data

Methods

n/a	Involved in the study
☒	☐ ChIP-seq
☒	☐ Flow cytometry
☒	☐ MRI-based neuroimaging